The Mars Regional Atmospheric Modeling System: Model Description and Selected Simulations

Scot C. R. Rafkin

Department of Meteorology, San José State University, One Washington Square, San José, California 95192-0104
E-mail: rafkin@metsunl.sjsu.edu

Robert M. Haberle

Space Science Division, Mail Stop 245-3, NASA Ames Research Center, Moffett Field, California 94035-1000

and

Timothy I. Michaels

Department of Meteorology, San José State University, One Washington Square, San José, California 95192-0104

The Mars regional atmospheric modeling system (MRAMS) is introduced, and selected model results are presented and compared with landed meteorological data when possible. MRAMS is descended from a nonhydrostatic Earth mesoscale and cloud-scale model that is widely used for forecasting weather and simulating atmospheric systems over complex terrain. Mesoscale models such as MRAMS are ideal tools for making use of the high-resolution data sets arriving from Mars Global Surveyor experiments. Simulation of the Mars Pathfinder (MPF) landing site at $L_s = 142$ using $1/2$ degree Mars orbiter laser altimeter (MOLA)-derived topography and thermal emission spectrometer thermal inertia is shown to be in good agreement with observed near-surface temperature, pressure, and wind direction. Simulations of topographically induced thermal circulations and mountain-induced gravity waves are shown to be consistent with theory and earlier studies that tie large-amplitude mountain waves to strong winds capable of producing dust streaks and local dust-lifting events. A large eddy simulation of the convective boundary layer provides estimates of vertical profiles of heat flux, momentum flux, turbulent kinetic energy, and vertical velocity variance. The model results suggest that the martian atmosphere is roughly two to three times more turbulent than the terrestrial atmosphere during the afternoon, but fluxes are roughly an order of magnitude smaller due to the lower density. Dust-devil-like circulations are also predicted in the large eddy simulation. Finally, a simulation that examines atmosphere–surface interactions near Big Crater is discussed. Predicted surface wind stress patterns are consistent with aeolian processes inferred through Mars Orbiter Camera imagery of Big Crater, located near the MPF landing site. © 2001 Academic Press

Key Words: Mars, atmosphere; atmospheres, dynamics; atmospheres, structure; Mars, surface.

I. INTRODUCTION

There is a rich modeling history of the martian atmosphere. Over three decades ago, general circulation models (GCMs) designed for the Earth were adapted to Mars (Mintz 1961, Leovy and Mintz 1969). GCMs simulate large-scale circulations over the entire planet and over time scales of a season or more. When compared to remotely sensed and *in situ* observations of the martian atmosphere, GCMs generally produce favorable results and capture the essential features of the martian climate (e.g., Haberle *et al.* 1993b).

Due primarily to computational constraints, GCMs are run at horizontal grid spacings that poorly resolve or are completely incapable of resolving mesoscale features. GCMs do not resolve microscale circulations—these must be parameterized as are, for example, the microscale eddies in the convective boundary layer. A typical GCM simulation has a horizontal computational grid spacing on the order of 5 by 5 degrees. GCMs have been run at higher resolutions (1 by 1 degrees) and can approach what might be considered the coarse end of the mesoscale. As processing power increases it is not unreasonable to expect the GCMs to increase further in resolution.

GCMs are also limited by their dynamics, which assume a hydrostatically balanced atmosphere. Circulations that require large accelerations of the vertical wind cannot be properly modeled. These circulations include, for example, large amplitude nonhydrostatic mountain waves. Convective adjustment schemes are employed to keep GCMs from developing strong superadiabatic lapse rates that would lead to a violation of model assumptions (e.g., hydrostaticity). Consequently, the predicted boundary layer temperature and depth are often in error.

Despite the coarse resolution and dynamical constraints on GCMs, they have done a remarkably good job at reproducing much of the observed general circulation of the atmosphere e.g., Pollack *et al.* 1990, Haberle *et al.* 1993b, Wilson 1997), and many of the local circulations observed at the Mars Pathfinder (MPF) and Viking Landers 1 and 2 (e.g., Haberle *et al.* 1999, Lewis *et al.* 1999). Additionally, GCMs have proven invaluable for investigating the dynamics of the large-scale circulation, including planetary waves and baroclinic disturbances (Collins and James 1995, Collins *et al.* 1996), the energy transfer processes associated with the zonal mean flow and transient and stationary eddies (Barnes *et al.* 1993), the interaction of the disturbances with topography (Pollack *et al.* 1990), and tides (e.g., Wilson and Hamilton 1996, Bridger and Murphy 1998).

Images from the Viking missions and most recently from the Mars Global Surveyor (MGS) and Mars Pathfinder (MPF) make it clear that the martian atmosphere is quite active at the meso- and microscales. Obvious evidence for mesocale processes is the so-called light and dark streaks downwind of topographic barriers, particularly craters, ridges, and isolated hills (Greeley *et al.* 1974, Veverka *et al.* 1981, Thomas *et al.* 1984, Thomas 1984). An example of these features is shown in Fig. 1, which are Mars Orbiter camera (MOC) images from the eastern slopes of Tharsis (MOC images M0303926 and M0300823). It is believed that these features result from removal or deposition of dust as the atmosphere impinges on the topographic barriers (Veverka 1975, Magalhães and Young 1995). There are also streaks that appear to be unassociated with any obstacle but are correlated with long slopes of $1°$ to $10°$ (Magalhães and Gierasch 1982).

Some of the wind streaks are of such small scale that they may be classified as resulting from microscale circulations produced by the interaction of the airflow with the topographic obstacle. To complicate matters further, the background airflow in which the microscale circulations are embedded may be of mesoscale origin. Evidence of microscale circulations can also be found in the map of aeolian features at the MPF as reported by Greeley *et al.* (1999) and Bridges *et al.* (1999). Many of these features show evidence of multiple wind regimes, some of which are inconsistent with GCM predicted winds. The inconsistent features may be signatures of paleoclimatic wind regimes or may result from local and intermittent wind regimes, which can only be simulated by a model with significantly greater spatial and temporal resolution.

Perhaps the most dynamically exciting features observed in the Mars atmosphere is the dust devil (Metzger *et al.* 1999). These whirlwinds may play a critical role in the maintenance of the background atmospheric dust load. Atmospheric dust strongly forces the climate and general circulation of the atmosphere, and it impacts exploratory mission operations. Unfortunately, the dynamics of dust devils in the highly unstable convective boundary layer are poorly understood.

Many investigators have developed a variety of one- and two-dimensional models (numerical and theoretical) that can be applied with validity to investigate phenomena that GCMs cannot resolve or are unable to reproduce due to assumptions in model dynamics. These mesoscale studies have been restricted primarily to slope flows and thermally induced polar cap circulations.

With respect to slope flows, Magalhães and Gierasch (1982) developed an analytical, two-dimensional nighttime model of slope winds in an attempt to explain the dark, erosion streaks on the slopes in the Tharsis and Elysium regions. Their results indicated friction velocities may approach the threshold velocity of $\sim$2 m/s required to initiate saltation (Greeley *et al.* 1980) but generally are less than 1 m/s. Steep slopes, large coefficients of drag, and very cold surface temperatures are required to produce the largest friction velocities. Ye *et al.* (1990) produced a comparative theoretical and modeling study of upslope flows on Mars and Earth valid during the daytime. They found that the upslope flows on Mars are typically two to three times larger than on Earth and extend to much greater depths (5 km). Friction velocities remained well below 1 m/s in all the simulations. Savijärvi and Siili (1993) conducted two-dimensional numerical simulations of martian slope flows and the nocturnal jet. Their results indicated the development of a jet similar to that found on the high plains of the United States.

With respect to polar cap studies, the Finnish research group has applied their two-dimensional hydrostatic code to investigate winds and surface stresses under varying atmospheric dust opacities at the southern polar cap edge (Siili *et al.* 1997). This study perhaps represents the use of the most dynamically complex mesoscale model in the published literature.

Given the large number of mesoscale and microscale atmospheric phenomena and processes in the martian atmosphere, and the important feedback processes which couple the micro- and mesoscale to the general circulation (e.g., the dust cycle), we have undertaken the development of a three-dimensional numerical model capable of simulating these phenomena. We present here the model description and selected results from the Mars regional atmospheric modeling system (MRAMS).

MRAMS is a versatile numerical model of Mars' atmosphere. MRAMS is descended from the regional atmospheric modeling system (RAMS), which is a widely used Earth model (Pielke *et al.* 1992) designed to simulate synoptic-scale, mesoscale, and microscale atmospheric flows over complex topography. As such, MRAMS is the ideal tool for utilizing the high-resolution products from the Mars Global Surveyor (MGS); the resolution of the data and MRAMS are compatible. The details of the MRAMS physics are presented in the next section, followed in subsequent sections by presentations of modeling results from the following numerical experiments that have benefited from MGS-derived data: (1) the Mars Pathfinder landing site (MPFLS) with comparison to observations; (2) thermal circulations and mountain waves; (3) atmosphere–surface interactions over a crater similar to Big Crater at MPF; and (4) an idealized large
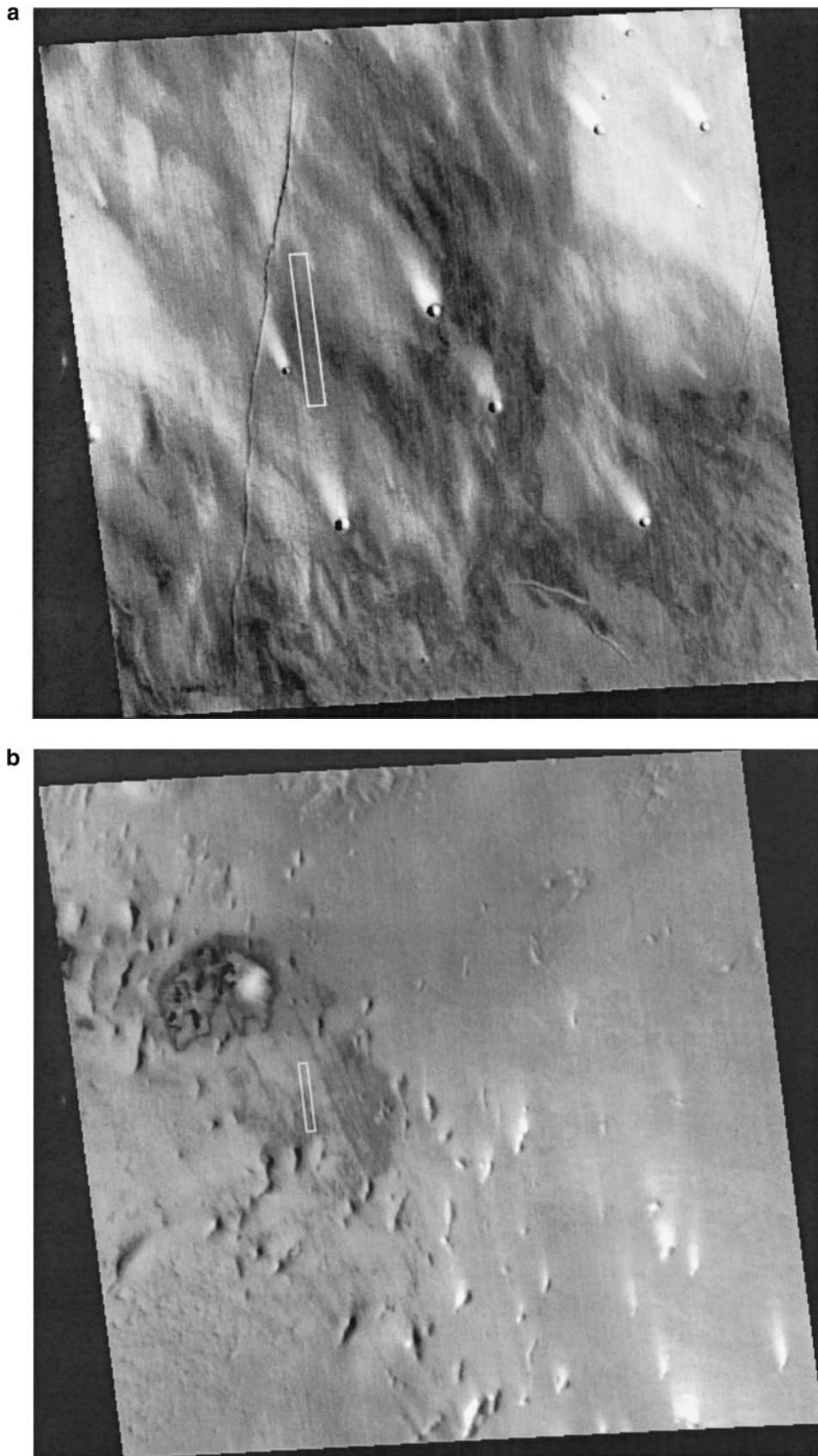
FIG. 1. MOC images of (a) crater dust streaks (image M0303926) and (b) dust streaks in the lee of small ridges and hills (image M0300823).

eddy simulation (LES) that includes dust-devil-like circulations.

II. MODEL DESCRIPTION

Definitions and values for the variables and constants in this and subsequent sections may be found in the Appendix.

A. Governing Equations

MRAMS is based upon the grid-volume Reynolds-averaged primitive equations

$$\frac{D\bar{u}}{Dt} = f\bar{v} - \theta\frac{\partial\pi'}{\partial x} + \nabla\cdot(K_m\nabla\bar{u}) \tag{1}$$

$$\frac{D\bar{v}}{Dt} = -f\bar{u} - \theta\frac{\partial\pi'}{\partial y} + \nabla\cdot(K_m\nabla\bar{v}) \tag{2}$$

$$\frac{D\bar{w}}{Dt} = -\bar{\theta}\frac{\partial\pi'}{\partial z} - g\frac{\theta'}{\theta_o} + \nabla\cdot(K_m\nabla\bar{w}) \tag{3}$$

$$\frac{D\bar{\theta}}{Dt} = \nabla\cdot(K_h\nabla\bar{\theta}) + \left.\frac{\partial\bar{\theta}}{\partial t}\right|_{Diabatic} \tag{4}$$

$$\frac{D\bar{r}}{Dt} = \nabla\cdot(K_h\nabla\bar{r}) + \left.\frac{\partial\bar{r}}{\partial t}\right|_{source/\sin k} \tag{5}$$

$$\frac{D\pi'}{Dt} = \frac{c_s^2}{\rho_o\theta_o^2}\nabla\cdot\rho\bar{V}\theta_o. \tag{6}$$

In Eqs. (1) through (6) the variables have been decomposed into a base state $(\ )_o$, a resolved perturbation from the base state $(\ )'$, and an unresolved fluctuating turbulent component $(\ )''$. For example,

$$\theta = \theta_o + \theta' + \theta'' = \bar{\theta} + \theta''. \tag{7}$$

Upon Reynolds averaging Eq. (7), the turbulent component vanishes. Reynolds averages of variances and covariances of unresolved fluctuating turbulent variables do not vanish and are modeled via diffusive eddy terms. The basic state is assumed to be hydrostatic and dynamically balanced.

Equations (1) through (3) are the momentum equations with the pressure gradient term cast in terms of the potential temperature, θ, and the Exner function, π, which are defined as

$$\theta = T\left(\frac{p_o}{p}\right)^{\frac{R}{c_p}} \tag{8}$$

and

$$c_pT = \pi\theta, \tag{9}$$

respectively.

Equation (4) is the thermodynamic equation. Potential temperature is conserved in the absence of diabatic heating terms. At present diabatic heating is possible through radiative forcing and through atmosphere–surface heat exchange as dictated by the atmospheric surface layer parameterization. Latent heating is not yet included in the model. We intend to develop appropriate microphysical schemes in the near future.

Equation (5) governs the behavior of tracers. MRAMS can handle up to approximately 100 individual tracers that the user may initialize heterogeneously in space. Additionally, the user can easily define sources and sinks for the tracers so that chemical modeling and/or deposition of tracers can be accomplished.

Finally, Eq. (6) governs conservation of mass and allows for compressibility of the atmosphere. Clearly, acoustic waves will be a solution to Eqs. (1) through (6). The numerical techniques for dealing with this are discussed below.

B. Parameterizations

1. Turbulent Mixing

The following description of the turbulence parameterizations follows from the *RAMS Technical Description* (Mission Research Corporation Aster Division, P.O. Box 466, Fort Collins, Colorado 80522). MRAMS assumes that turbulent mixing may be expressed by parameterizing the turbulent flux of scalars as a constant multiplied by the gradient of the quantity being transported,

$$\overline{u_n'\chi'} = -\hat{n}\cdot\mathbf{K}_h\frac{\partial\bar{\chi}}{\partial x_n}, \tag{10}$$

where $\mathbf{K}_h$ is the vector horizontal mixing coefficient for scalar species (with components in each horizontal direction) and $\hat{n}$ is the unit vector in the direction of mixing transport. The turbulent tendency to the resolved scalars is given by the flux convergence of the Reynolds stress:

$$\left.\frac{\partial\bar{\chi}}{\partial t}\right|_{turbulence} = \frac{\partial}{\partial x_n}(\overline{u_n'\chi'}). \tag{11}$$

The turbulent tendency for momentum is similar to Eq. (11):

$$\left.\frac{\partial\bar{u}_i}{\partial t}\right|_{turbulence} = \frac{\partial}{\partial x_n}(\overline{u_n'u_i'}). \tag{12}$$

The expression for the momentum fluxes in Eq. (12) are generally not expressed as simply as for scalars (Eq. 10). When the horizontal grid spacing is significantly greater than the vertical grid spacing, the expression used in the horizontal (i and $j = 1$, 2) is

$$\overline{u_i'u_j'} = -\hat{i}\cdot\mathbf{K}_m\left(\frac{\partial\bar{u}_i}{\partial x_j} + \frac{\partial\bar{u}_j}{\partial x_i}\right), \tag{13}$$

where $\mathbf{K}_m$ is the momentum mixing coefficient vector. In the vertical direction (i or $j = 3$), the following expression is usually

used:

$$\overline{u'_i u'_j} = -\hat{i} \cdot \mathbf{K}_m \frac{\partial \bar{u}_i}{\partial x_j}. \qquad (14)$$

However, when the horizontal and vertical grid spacing are of comparable magnitude, Eq. (13) is used for all directions (i and $j = 1, 2, 3$) in place of Eq. (14). The user may specify which formulation is used, so it is possible although not recommended to use Eq. (14) when the horizontal grid spacing is larger than the vertical, or vice versa with Eq. (13). The difference in the formulations results from the assumption that convective motions are resolved when the horizontal and vertical grid spacings are of comparable scale and when the grid spacing is sufficiently small to capture the circulations. When the horizontal and vertical spacing differ, and the convective motions are not resolved, artificially large diffusion is needed for numerical stability and to reproduce the vertical mixing that is not resolved. Note that Eq. (14) does not require symmetry of the stress tensor: $\overline{u'_i u'_j} \neq \overline{u'_i u'_j}$ in general. The stress tensor is symmetric in the formulation Eq. (13).

The mixing coefficients may be diagnosed four different ways depending upon the user's preference. Two of the schemes are high-order closures which prognose turbulent kinetic energy (TKE) and use TKE to determine the mixing coefficients (Mellor and Yamada 1982, Deardorff 1972). The remaining two schemes are lower order closures based upon the local strain and deformation (Smagorinsky 1963).

When the horizontal grid spacing is small, the eddy mixing coefficient for the low-order closure is written

$$\mathbf{K}_m \cdot \hat{\mathbf{n}} = \rho C_x \Delta x C_z \Delta z \{S_3 + F_H [\max(0, -N^2)]^{0.5}\}$$
$$\times [\max(0, 1 - \alpha R_i)]^{0.5}, \qquad (15)$$

where

$$\mathbf{K}_h = \alpha \mathbf{K}_m. \qquad (16)$$

C_x and C_z are coefficients, which multiply the grid spacing to obtain the horizontal and vertical mixing length scales, respectively. Canonically, these coefficients are given a value of 0.2 F_H may be set to 0 or 1 to activate an optional enhancement of vertical mixing proportional to the Brunt–Vaisala frequency (N^2) in convectively unstable cases. R_i is the Richardson number and α is the ratio of the scalar to momentum mixing coefficients, which is specified by the user (canonically set to 3.0). Finally, S_3 is the magnitude of the rate-of-strain tensor, the components of which are given by the bracketed term on the right-hand side of Eq. (13).

For larger grid spacings, the low-order closure for the horizontal mixing coefficient is

$$\mathbf{K}_m \cdot \hat{\mathbf{n}} = \rho_o \max[K^*, (C_x \Delta x)^2 \{S_H\}^{0.5}], \qquad (17)$$

where $\hat{\mathbf{n}}$ is either $\hat{\mathbf{i}}$ or $\hat{\mathbf{j}}$. K^* is a minimum value of the horizontal momentum mixing coefficient given by

$$K^* = 0.075 K_A (\Delta x^{4/3}), \qquad (18)$$

where K_A is a user-specified coefficient with a canonical value of 1.0. S_H is the magnitude of the rate-of-strain tensor computed setting all terms with a vertical element ($i, j = 3$) equal to zero.

The low-order closure for the vertical mixing coefficients is as given by Eq. (15), but z replaces x for all terms and S_1 replaces S_3 and is given by the magnitude of the right-hand side of Eq. (13) with $i = 1, 2$ and $j = 3$.

The higher order closures involve the prognostication of turbulent kinetic energy (TKE). TKE is advected as a tracer in the model so that the mixing coefficients are based upon TKE generated or dissipated locally plus that advected into the grid box. A modified form of the closure proposed by Mellor and Yamada (1982) is used to compute the vertical mixing coefficients when the horizontal grid spacing is large. The horizontal scheme remains the same as for the low-order closure.

The prognostic equation for TKE is given by

$$\frac{D\bar{e}}{Dt} = \nabla \cdot (K_e \nabla \bar{e}) + SHEAR + BUOY + DIS, \qquad (19)$$

where e is TKE, and *SHEAR*, *BUOY*, and *DIS* are shear production, buoyancy generation, and dissipation of TKE, respectively. The formulation of these source and sink terms follows that of Mellor and Yamada's (1982) level 2.5 closure scheme.

The shear production is given by

$$SHEAR = K_m \left[\left(\frac{\partial u}{\partial x} \right)^2 + \left(\frac{\partial v}{\partial y} \right)^2 \right]. \qquad (20)$$

The buoyancy production term is given by the product of the horizontal scalar mixing coefficient (K_h) with the Brunt–Vaisala frequency, and the dissipation term is given by

$$DIS = a_\varepsilon e^{1.5} l^{-1}. \qquad (21)$$

The turbulent length scale, l, is given by

$$l = \frac{k(z + z_o)}{1 + k(z + z_o)/l_\infty} \qquad (22)$$

and

$$l_\infty = 0.1 \frac{\int_0^H z \sqrt{e} \, dz}{\int_0^H \sqrt{e} \, dz}, \qquad (23)$$

where k is the Von Karman constant, z_o is the roughness length, and H is the top of the model. The length scale in stable conditions

is clipped following Andre *et al.* (1978) so that

$$l \leq 0.75 \left[\frac{2e}{N^2} \right]^{0.5}. \tag{24}$$

The mixing coefficients are obtained from the expressions

$$
\begin{aligned}
K_m &= S_m l \sqrt{2e} \\
K_h &= S_h l \sqrt{2e} \\
K_e &= S_e l \sqrt{2e},
\end{aligned}
\tag{25}
$$

where S_h and S_m are algebraic expressions involving vertical gradients of u, v, and θ nondimensionalized by turbulent kinetic energy and the mixing length.

2. Radiation

The radiation parameterization in MRAMS is taken from the NASA Ames general circulation model as described by Haberle *et al.* (1999) and Pollack *et al.* (1990). The parameterization includes the radiative effects of CO_2 gas, suspended dust, and water ice clouds at both thermal and infrared wavelengths. Cloud microphysics are not yet active in MRAMS so that the radiative effect of clouds is currently not considered. The MRAMS version of the radiation parameterization presently requires the user to specify a fixed dust optical depth, which is uniform across the domain at a given pressure (611 Pa). Future versions of the model will account for variable dust concentrations via advection, dust-lifting, and deposition.

As described by Pollack *et al.* (1990), many of the radiation calculations are done off-line, the results of which are utilized by the radiation parameterization via cubic spline interpolation from multidimensional look-up tables. At solar wavelengths, heating due to the absorption of CO_2 gas is computed first. The remaining flux is used to calculate heating by dust. The two heating rates are then added together. CO_2 absorption is based on equivalent width formulae for the near infrared CO_2 bands. For dust, a net solar flux table is generated off-line using a doubling code and scattering properties determined from Viking Lander sky brightness measurements. The net flux depends on total dust optical depth, dust optical depth to the level in question, solar zenith angle, and albedo.

Infrared heating is calculated within and outside the 15 μm CO_2 band. Within the 15 μm band, dust and CO_2 gas emissivities are calculated and then combined assuming no spectral correlation. Outside the 15 μm band, only dust contributes to the radiation fields. Dust emissivities were calculated off-line using a two-stream code and assuming the single scattering properties described in Haberle *et al.* (1982). Emissivities for CO_2 were obtained by performing line-by-line calculations for a wide range of temperatures and pressures, which were then placed in a multidimensional look-up table.

3. Surface Layer

The flux of heat and momentum from the surface to the atmosphere adheres to the basic principles of Monin–Obukhov similarity theory as described by Louis (1979) following the earlier work of Bussinger (1971). The solution typically requires an iterative solution (Lewellen and Teske 1973), but a noniterative analytic approximation described by Manton and Cotton (1977) is used in MRAMS. The heat and momentum fluxes are written as

$$u_* \theta_* = a^2 u \, \Delta\theta F_h \left(\frac{z}{z_o}, Ri \right) \tag{26}$$

$$u_*^2 = a^2 u^2 F_m \left(\frac{z}{z_o}, Ri \right), \tag{27}$$

where

$$a^2 = \frac{k^2}{\left(\ln \left(\frac{z}{z_o} \right) \right)^2}, \tag{28}$$

and $\Delta\theta$ is the difference between the lowest level model atmosphere potential temperature and the ground temperature. $F_{m,h}$ are functions of the Richardson number, normalized model height, and empirically determined constants. The functions are modified for stable versus unstable conditions. As in the case of many of the constants in the turbulence closure, the constants supplied here assume universality or a similarity to Earth.

4. Soil Model

The soil model assumes that energy transfer below the surface is due solely to conduction. At the atmosphere–soil interface, radiation and turbulent energy fluxes also contribute. The energy flux at level z below the surface is given by

$$F(z \neq 0) = k \frac{\partial T_s}{\partial z}. \tag{29}$$

The flux at the surface is given by

$$F(z = 0) = \varepsilon \sigma T_s^4 + (1 - \alpha) SW \downarrow + LW \downarrow + k \frac{\partial T_s}{\partial z} + \overline{w'T'}, \tag{30}$$

where T_s is the soil temperature, α is the soil albedo, k is the thermal conductivity, and ε is the soil emissivity. The short and long wave radiation fluxes are provided by the radiation parameterization, and the turbulent heat flux is provided by the surface layer parameterization. The change in soil temperature is then given by

$$\frac{\partial T_s}{\partial t} = -\frac{1}{\rho C_p} \frac{\partial F}{\partial z}. \tag{31}$$

Note: the density and heat capacity in Eq. (31) refer to that of the soil and not the atmosphere. The conductivity, density, and heat capacity can be specified as constant throughout the soil, given a vertical variation, or they can be varied horizontally and vertically. The square root of the product of conductivity and volumetric heat capacity is the soil thermal inertia, which is thought to vary by over an order of magnitude from 20 to 400 units over the surface of the planet. Thermal conductivity is retrieved by taking the thermal emission spectrometer (TES) thermal inertia data set and fixing volumetric heat capacity at a constant value. Fixing the heat capacity and solving for conductivity was chosen over fixing the conductivity and solving for the heat capacity since the conductivity is thought to vary more widely than the heat capacity (Christiansen and Moore 1992). The soil albedo is usually obtained by interpolation from the Mars Consortium data set, although any gridded data set can be used.

Presently, the effect of CO_2 phase changes at the ground are not considered in the surface heat budget. This limits the applicability of the model in regions where this process is important. A surface sublimation/deposition scheme is expected in future versions of the model.

C. Computational Grids

All MRAMS computational grids are of the Arakawa C-type as shown in Fig. 2. Thermodynamic variables and tracer species are staggered by one-half a vertical grid box below the vertical velocity, and the u and v wind components are at the same level as the thermodynamic variables but staggered horizontally by one-half of a horizontal grid box.

Unlike most GCMs, the MRAMS grid is not regularly spaced in latitude and longitude. Instead, the modeling domain is projected onto an oblique polar–stereographic projection with con-

stant linear distance spacing on the projection. Consequently, the actual domain is an irregularly spaced grid, and map scaling factors must be included in all horizontal derivatives. The pole point of the projection is user specified, but generally lies close to the center of the domain. Also, the domain is regional not global.

The vertical coordinate is a terrain-influenced sigma-z coordinate defined by

$$\sigma(z) = H\left(\frac{z - Z_T}{H - Z_T}\right), \tag{32}$$

where H is the height of the model top and Z_T is the topographical height based upon the reference geoid. The vertical grid spacing is user specified and is generally prescribed a constant geometrical stretching factor defined as the ratio of the grid spacing between adjacent vertical levels. Setting the ration to 1.0 provides a uniformly spaced vertical domain. Typically, values between 1.0 and 1.2 are used to provide a higher density of vertical levels near the surface. Finally, a maximum vertical grid spacing is often prescribed to prevent the geometrical stretching from generating undesirably large grid spacing at high levels. In some situations, it may be desirable to have high vertical resolution at locations other than near the surface. Consequently, the user may also specify the model levels explicitly.

MRAMS has two-way interactive nested grids (Clark and Farley 1984). A nested grid is a grid of finer grid spacing that lies within a coarser parent grid. The physics are solved first on the parent grid and then on the fine grid using the parent grid values as boundary conditions. In the cases where a smaller time step is used on the fine grid, the parent grid values supplying the boundary condition are linearly interpolated in time.

Two-way nesting involves sending back to the parent grid the averaged fine grid solution. Nested grids allow the user to concentrate computational power where it is needed, while simultaneously saving computational time where it is not. Nesting is typically done horizontally, but vertical nesting, or a combination of both, may be selected.

An infinite number of nested grids may be utilized in an MRAMS simulation, but there is a practical limit. Since the Courant–Friedrichs–Levy (CFL) stability condition is a function of grid spacing, the model time step on each nested grid is generally reduced from the parent grid value, and the reduction must be an integral factor. For each parent grid model time step, the physics must be solved two or three times on the nested grid. In practice, computational speed limits the number of nested grids to 5 or 6, which can involve 20 or more innermost nest time steps for the outermost nest time step.

D. Computational Techniques

1. Integration

Acoustic and gravity waves are solutions to the model equations. Direct integration of the equations would require a time step adequate to prevent numerical instability associated with
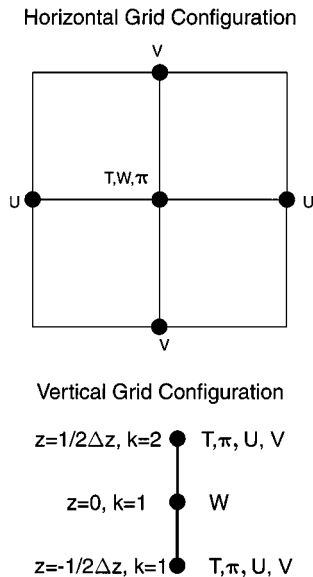
Horizontal Grid Configuration

Vertical Grid Configuration

$z=1/2\Delta z$, k=2 ● T,π, U, V

$z=0$, k=1 ● W

$z=-1/2\Delta z$, k=1 ● T,π, U, V

FIG. 2. The MRAMS computational grid based upon an Arakawa C-type grid.

these fast waves. To improve model efficiency, the dynamical equations are split into two sets of equations. The first set has as its solutions the fast waves and is solved over a short time step. The second set represents the slow solutions and is solved over a longer time step that is an integer multiple of the short time step. Although retaining the acoustic mode in the equations may seem computationally inefficient, removing sound waves through, for example, the anelastic approximation requires the solution of a complicated elliptical equation for pressure (Pielke 1984). The costs of retaining acoustic waves and solving the elliptic pressure equation are comparable. The details of this procedure may be found in Tripoli and Cotton (1982) and Klemp and Wilhelmson (1978).

Integration of the model equations in time and space is performed using forward time differencing of potential temperature, and leapfrog differencing of π and velocity. Advection is done by casting the advection term in mass flux form to better conserve mass and momentum. The user may choose between a second- or sixth-order forward advection operator as described by Tremback *et al.* (1987).

2. Initialization and Boundary Conditions

a. Horizontal homogeneity. MRAMS may be initialized in two different ways. First, the atmospheric domain may be initialized horizontally homogeneously based upon a single sounding. In this case atmospheric properties are constant along a constant height surface throughout the domain. If topography is included in this type of simulation, the higher topography will intersect the homogeneous atmospheric layers resulting in gradients along the surface. The single initialization is often beneficial for conducting idealized simulations.

The user may choose a variety of boundary conditions when a horizontally homogeneous initialization is selected. The wind component normal to the horizontal boundary is obtained from the radiative boundary condition

$$\frac{\partial u}{\partial t} = -(u + c)\frac{\partial u}{\partial x}, \qquad (33)$$

where u is the normal velocity component and c is a phase speed.

The phase speed, c, may be selected in four ways. The simplest form is for the user to set the phase speed. Typically a value in the range of gravity wave phase speed propagation is selected, which should allow for gravity waves to exit the domain with a minimum amount of reflection. The second method is to set the phase speed equal to the ratio of the time derivative to the spatial derivative following Orlanski (1976). Another possibility is to assign the phase speed the vertically integrated average of the phase speed computed with the Orlanski method. The final possibility is to use cyclic boundary conditions. The latter condition is most often used for large eddy simulations. When using cyclic boundary conditions, topography and other forcings must be periodic within the domain to prevent discontinuity (and most likely a dominance of nonphysical model solutions). The

first method of choosing a phase speed is typically selected, with the other options being employed if significant boundary noise develops, or if a cyclic simulation is desired.

Variables other than the normal component of velocity are prescribed in one of four ways: (1) zero gradient inflow and outflow; (2) zero gradient inflow and radiative outflow; (3) constant inflow and radiative outflow; (4) constant inflow and outflow. The first option is typically selected.

Vertical velocity may be set to zero at the model top (a wall). Alternatively, a radiative condition may be applied, which reduces the reflection of gravity waves propagating through the domain boundary. Whether selecting a wall or radiative boundary, an absorbing (sponge) layer may be applied. The absorbing layer relaxes the variable back to the base state over a variable time scale and over a user-determined absorbing layer. The user specifies the minimum time scale, which is valid at the model top. The time scale increases linearly to an effective value of infinity at the bottom of the absorbing layer. In the single sounding initialization, the base state is constant in time.

b. Variable initialization. The second method by which MRAMS may be initialized is through a variable initialization technique in which one or more data sets are blended and interpolated to the computational domain. When variable initialization is selected, time-dependent boundary conditions must also be computed from data rather than numerically specified as is done with the homogeneous initialization.

The isentropic analysis (ISAN) package is front-end code to MRAMS that objectively analyzes and interpolates data to the MRAMS computational domain. Three basic types of data may be ingested by ISAN: gridded, sounding, or point observations. The standard gridded data input is from the NASA Ames general circulation model. The GCM data is on σ-pressure surfaces. These data are then horizontally interpolated to the MRAMS polar stereographic projection via a bilinear interpolation scheme. The topography for MRAMS is locally higher or lower than the GCM because MRAMS is at higher resolution and utilizes a higher resolution topographical data set. Consequently, the vertical mapping of the GCM data to MRAMS is more involved than the horizontal interpolation. The vertical interpolation to the MRAMS coordinate has been modified from the original terrestrial code as follows: Potential temperature and wind components in MRAMS are determined using the transformation

$$\chi_R(Z) = \chi_G[Z - \delta(Z)], \qquad (34)$$

where

$$\delta(Z) = -(Z - h)\frac{(\Delta_{topo})}{H} \qquad (35)$$

and

$$h = H + topo_R. \qquad (36)$$

χ is the model variable undergoing transformation, Z is the height above the geoid, Δ_{topo} is the difference between MRAMS and GCM topography, $topo_R$ is the height of MRAMS topography above the geoid, and H is a distance above the topography of MRAMS where the MRAMS and GCM properties are assumed identical. When $Z > h$, δ is set to 0. It can be seen that for $Z = topo_R$ (the surface in MRAMS) that $\delta = \Delta_{topo}$, and the surface value in MRAMS is set equal to the surface value in the GCM. When $Z = h$, then $\delta = 0$, and the MRAMS value at Z above the geoid is equal to the GCM value at Z above the geoid The net effect is a transformation where the atmospheric structure near the surface in the GCM is preserved in the translation to the MRAMS coordinate. This transformation is applied to T, U, and V. The pressure on the MRAMS grid is obtained by a hydrostatic integration downward from the model top where MRAMS and GCM pressure are identical.

The terrestrial vertical interpolation scheme was modified in the manner described above because the original scheme employed isentropic analysis (and thus, the term ISAN). While isentropic analysis is suitable for Earth, it is not appropriate for an atmosphere that becomes highly stable at night and superadiabatic during the day. Furthermore, the terrestrial code assumed a "standard" lapse rate for reduction of data to model heights located below the observational or gridded data. The lapse rate on Mars is highly variable and utilizing a "standard" lapse rate on Mars (assuming one could define one) would be highly suspect.

Sounding information, such as that which may be derived from remote sensing instruments, or surface observations can be included in the analysis. However, the sounding and surface data must be consistent with the gridded data from the GCM. In general, this requirement precludes the use of observed atmospheric data (e.g, TES and Radio Science) with the gridded GCM data; the GCM data represent the instantaneous state of the atmosphere in the GCM, while observational data represent the actual instantaneous state of the atmosphere. Single sounding initializations using TES or Radio Science can be conducted as previously discussed.

Lateral boundary conditions are obtained following Davies (1983). The user selects a boundary region (specified as a number of grid points) over which the model fields will be nudged towards the gridded analysis file. The strength of the weighting is a function of a user-selected time scale, and distance from the boundary. Points closest to the boundary are nudged more strongly than interior points within the boundary region. A similar technique is used for the top boundary.

III. NUMERICAL SIMULATIONS

A. Mars Pathfinder Landing Site

The increased data resolution of Mars' surface characteristics obtained by the Mars Global Surveyor are well suited for use in high resolution models such as MRAMS. The meteoro-

logical surface observations from the Mars Pathfinder landing site (MPFLS) make a mesoscale modeling study of the region a candidate for evaluation of model performance and model validation.

The MPFLS simulation presented here utilizes 1/2 degree Mars orbiter laser altimeter (MOLA) topographical data and 1/8 degree resolution thermal inertia. Presently, the surface albedo and roughness length are fixed at 0.16 and 5.0 cm, respectively. The albedo value is identical to the value at the MPFLS in the NASA Ames GCM simulation that was used to initialize the model. The surface roughness was selected somewhat arbitrarily and is based upon the subjective visual inspection of surface photographs at the landing site. The capability for varying these surface properties is a model feature, but this option was not utilized for this simulation. A constant soil density of $1790 \, kg/m^3$ and a soil specific heat capacity of $795 \, J \, kg^{-1} \, K^{-1}$ are used to obtain soil conductivity values from thermal inertia values as previously described.

The computational domain, centered on the MPFLS at ($19.33°$N, $33.55°$W), consists of 55×55 points in the horizontal with a grid spacing of 60 km and 47 points in the vertical with the lowest level at 7 m above the surface. The vertical grid spacing is gradually stretched with height from 15 m near the surface to a maximum spacing of 750 m. The total height of the domain is approximately 22 km.

All references to time in this simulation and those that follow are in Mars sols or hours unless explicitly stated otherwise. A Mars sol is taken to be 88,775.2 Earth seconds, and a Mars hour is taken to be 1/24 of a sol. Model time is the local time at the center of the modeling domain.

Initial fields and boundary conditions (imposed every six hours) for the simulation are obtained by processing output from the NASA Ames Mars GCM through ISAN (Figs. 3a–3c). The model run was started before sunrise (0530 local) at $L_s = 142$ and continued for approximately 3 sols. In order to evaluate model performance and validity, a portion of the Mars Pathfinder data set was used, roughly 4 sols in length and beginning at approximately $L_s = 142$. The dust optical depth of the MRAMS simulation was set identical to that used in the GCM simulation ($\tau = 0.3$) in order to maintain as much consistency as possible between the MRAMS solution and the initial and boundary conditions.

Comparing the temperatures observed by MPF and that predicted by MRAMS over time, it is clear that MRAMS slightly underpredicts the maximum temperature by about 5 K, but it is in better agreement with respect to the minimum temperature (Fig. 4). The difference in the maximum temperature may be entirely attributable to the extrapolation technique required to reduce the lowest model level ($\sim$7 m) to the Pathfinder observation level (1.27 m). A simple linear extrapolation based upon the modeled lapse rate was used. Realistically, the surface layer temperature profile is closer to exponential, which would suggest that the modeled maximum temperature is in much better agreement with the observations. The shape of the modeled
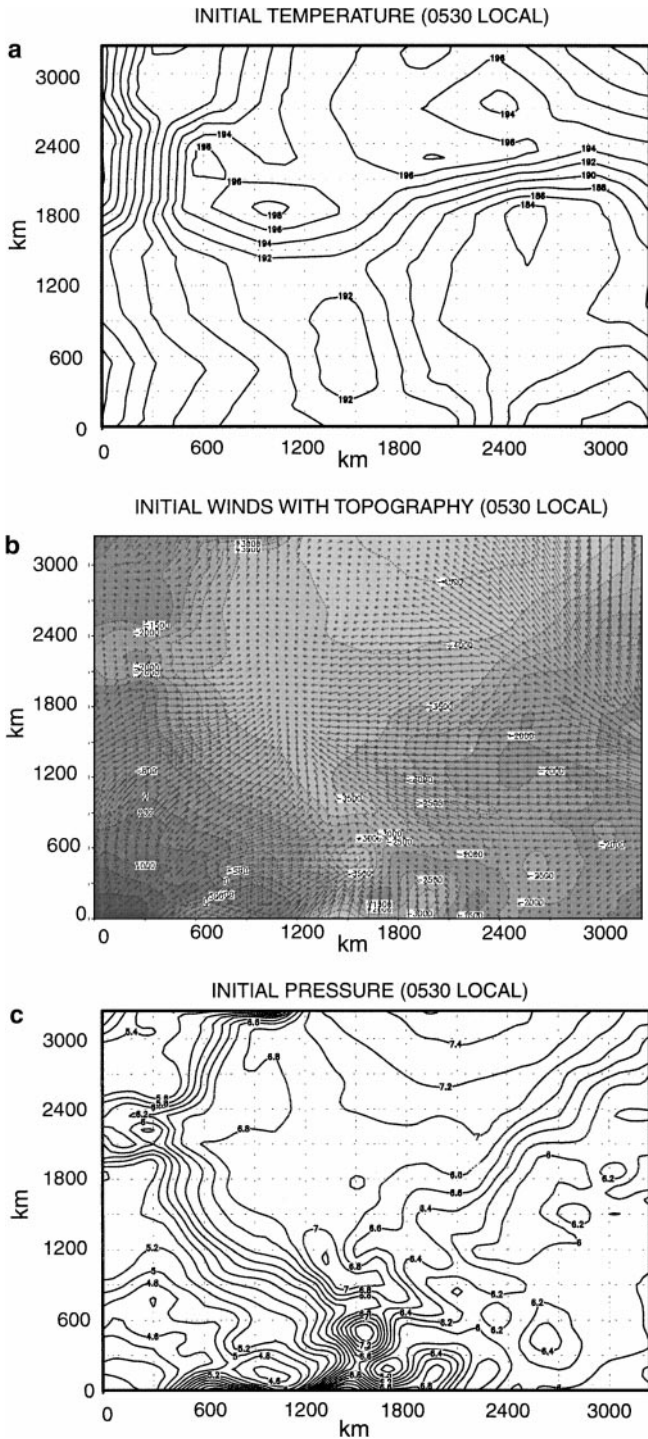
FIG. 3. Initial conditions derived by processing NASA Ames GCM gridded data through ISAN. a) surface temperature (K), b) wind vectors with underlying shaded topography (m), c) surface pressure (hPa). MPFLS is located in the middle of the domain.

temperature record is also in good agreement with observations, including the gradual cooling during the early morning hours and the occasional small departures in the hours prior to sunrise.

We note that in Fig. 4 the GCM temperature was not reduced to the observation height, which would have produced significantly better agreement with the observations. However, the GCM temperature record suffers from convective adjustment, which produces a noticeable "sharkfin" appearance. Since MRAMS is nonhydrostatic and does not utilize convective adjustment, the shape of the temperature record is more realistic.

Unfortunately, the small perturbations in modeled temperature in the early morning hours may be due to nonphysical behavior. We have found that the turbulent diffusion parameterization becomes increasingly ineffective as the stability increases. The turbulent mixing coefficents are so small prior to sunrise that mixing is strongly inhibited (a correct physical response). However, diffusion is also required to damp numerical instabilities. In the case of the MRAMS, the diffusion parameterization is unable to fully damp $2\,\Delta x$ noise (a nonphysical response). The early morning temperature record may be influenced by the insufficient numerical diffusion, although we suspect the perturbations are not entirely due to numerical noise. Complete removal of the $2\,\Delta x$ noise requires artificially increasing the diffusion beyond the predicted values, which has detrimental impacts on the results. For example, in a sensitivity experiment where mixing coefficients were kept artificially high, the predicted maximum temperature was reduced. We are presently exploring options and solutions to this dilemma (e.g., Forget *et al.* 1999).

A few experiments that test the sensitivity of temperature to changes in thermal inertia and albedo have been conducted. The results (not shown) indicate that a better agreement between the modeled and observed temperature may be obtained by adjusting these parameters. In particular, since we are diagnosing the soil diffusivity from the thermal inertia by holding soil density and heat capacity constant, there is considerable room for
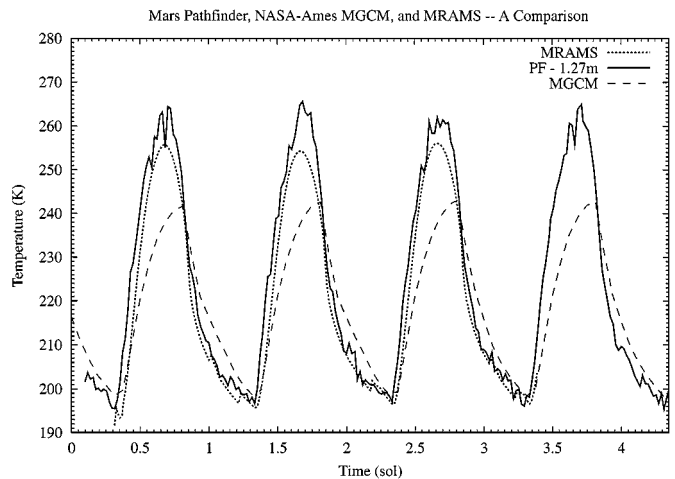
FIG. 4. Time series of temperatures from MPF ASI/MET experiment at 1.27 m, MRAMS with lapse rate extrapolation from 7 to 1.27 m, and GCM air temperature (~40 m) without reduction to surface. Sharkfin appearance of GCM temperature results from convective adjustment.
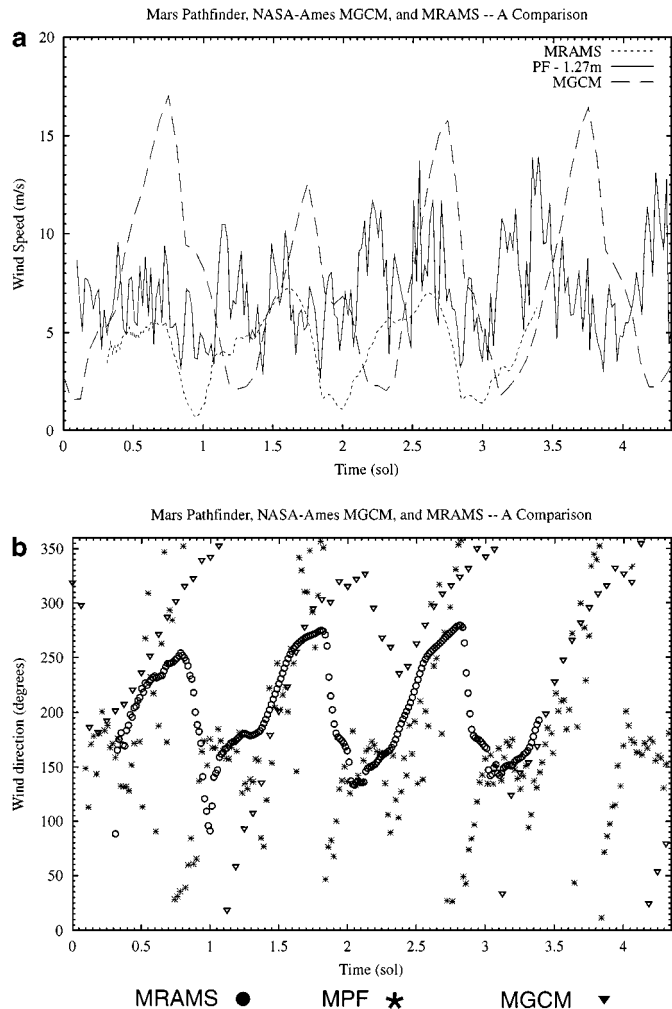
FIG. 5. Wind comparisons. Wind speed (a) from MRAMS lowest model level (short dash), MPF ASI/MET (solid), and GCM lowest model level (long dash). Wind direction (b) from MRAMS (short dash), MPF ASI/MET (solid), and GCM (long dash). NO elevation corrections were performed on model data. Accuracy of observational data is unknown (see text).

adjustment while simultaneously using the TES thermal inertia as a constraint. Our assumption of uniform density and heat capacity is clearly in error, although the magnitude of the error is unknown. An independent data set of soil density or heat capacity would be extremely useful and would help to eliminate the uncertainty. It is possible that the underprediction of temperature by MRAMS is due to a poor choice of albedo and thermal inertia rather than to a flaw in the temperature extrapolation.

MRAMS horizontal wind speeds are generally less than those observed (Fig. 5a). Wind data were obtained via a personal communication with J. Murphy (2000). These data are not highly reliable as wind retrieval algorithms for the ASI/MET data are still under development.

Possible reasons for the low model wind speeds include inaccurate observations for comparison, excessive friction caused

by too large a roughness length, and excessive model diffusion. We conducted a sensitivity study in which the roughness length was reduced to approximately 1.0 cm and we found only a small increase in the wind speed. Thus, roughness length cannot entirely account for the discrepancy between the model and the observations. The timing of the daily wind speed extrema is in agreement with MPF. Predicted wind direction agrees with observations until the atmosphere stabilizes after sunset (Fig. 5b). MPF data show the wind direction rotating a full 360 degrees per sol. Much of that rotation takes place within a few martian hours when the wind speed is low. That being the case, the simulated wind speed is near 0 at the time of the directional shift, which would mask the shift. The discrepancy may also be due to the errors involved in representing the MPFLS with the topographical data at 60 km grid spacing. For example, the model wind vector's two grid points to the south of MPF are turning in agreement with observations. Decreasing the model grid spacing may bring the model in better agreement with observations.

Atmospheric pressure as simulated in MRAMS resolves the general diurnal cycle (Fig. 6). The offset in mean pressure between the model and observations results from a difference in model topography from the actual elevation, and from the uncertainty in total atmospheric mass, which influences the initial and boundary conditions derived from the GCM. The MRAMS pressure cycle amplitude is smaller than observations, and semidiurnal tidal signatures are not represented. The NASA Ames GCM has had difficulty in reproducing the amplitude of the diurnal pressure cycle (Haberle *et al.* 1999). Since MRAMS utilizes the GCM output for boundary conditions and the GCM radiation code, it is not surprising that the MRAMS pressure amplitudes
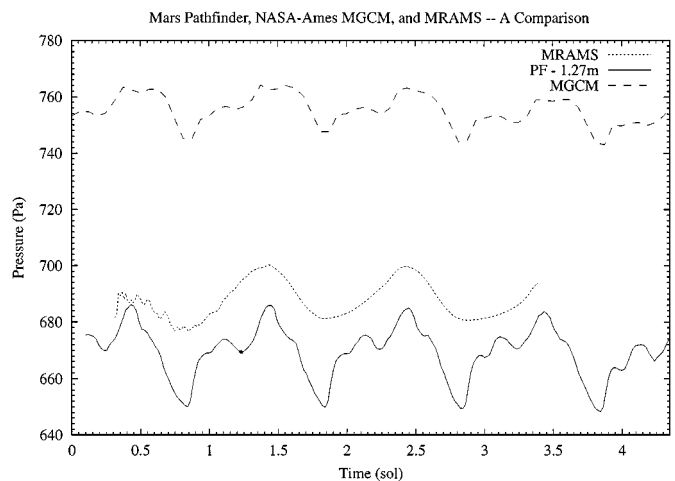
FIG. 6. Time series of surface pressure for MRAMS (short dash), GCM (long dash), and MPF/ASIMET (solid). The GCM and consequently MRAMS lacks the observed pressure cycle amplitude. MRAMS lacks a semidiurnal tidal component as expected from the smaller domain and aliasing of the tidal signature in the boundary conditions. Offsets result from differences in elevation between the models and observation.

are too small. It is also not surprising that MRAMS fails to capture the tidal signatures, since these are generated on a planetary scale well beyond the scope of the MRAMS domain. It may be possible to more closely represent tidal effects in MRAMS by supplying boundary conditions more frequently (e.g., every hour rather than every 6 hours). Alternatively, it may be possible to develop a tidal parameterization. It is also likely that tidal components have a small effect on the strongly forced mesoscale thermal and topographic circulations in which case the tides can be ignored to a good approximation.
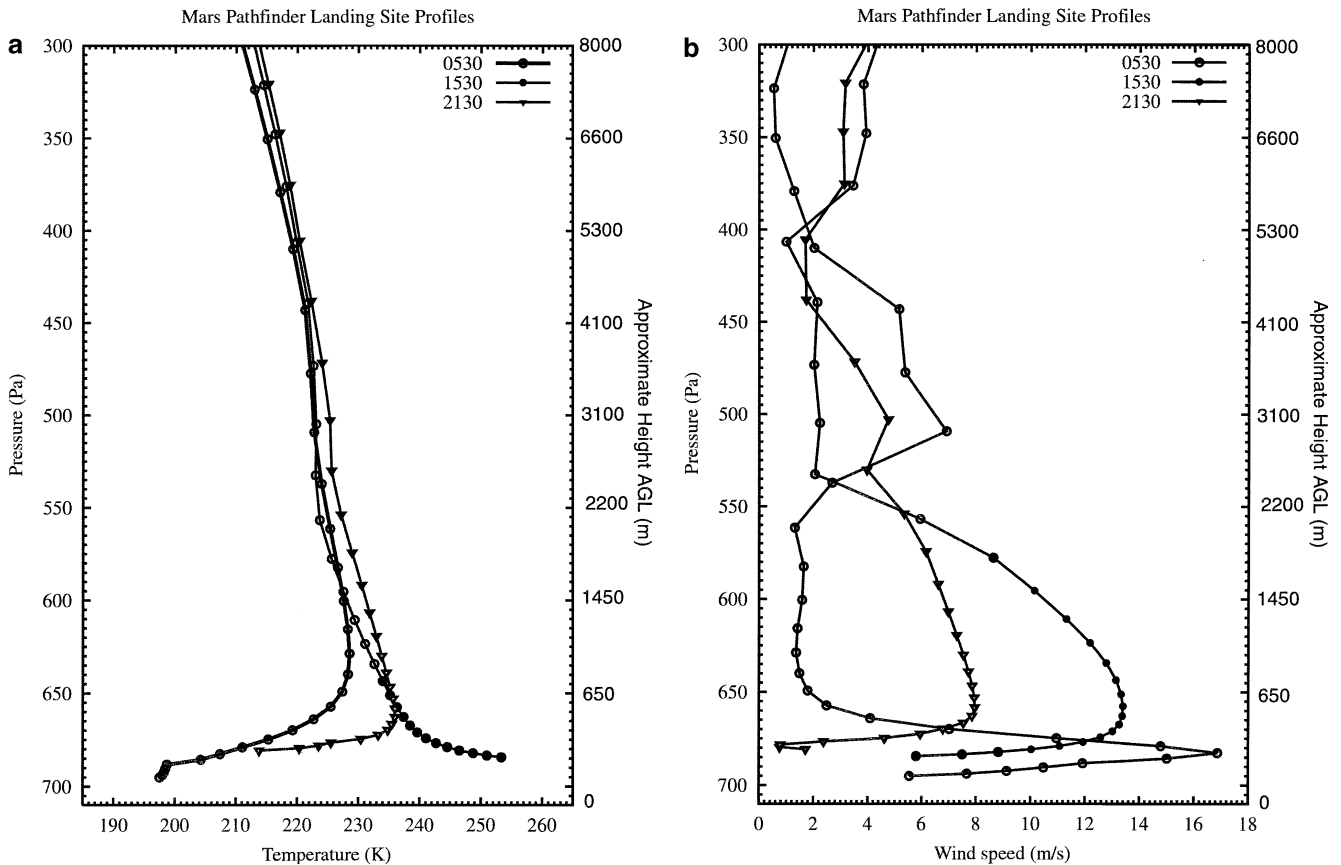
The vertical profile of temperature at selected times is shown in Fig. 7a. The model profiles are in general agreement with expectations and previous studies, most of which are at the Viking Lander 1 and 2 sites (Haberle *et al.* 1993, Seiff 1993, Seiff and Kirk 1977). The Pathfinder entry profile terminates at 8 km AGL and is therefore unavailable for comparison. At night, a strong radiation inversion is present. Radio occultations at 0400 local time are consistent with the model temperature profiles. The inversion is quickly eroded after sunrise. By midafternoon (1530 local), the low levels are superadiabatic to a depth of approximately 4 km. After sunset (2130 local), the radiation inversion

quickly redevelops leaving a nearly adiabatic residual mixed layer above.

An obvious feature in the profiles is the two-layer nocturnal inversion present in the early morning hours (0530 local). This feature develops gradually over time and indicates that while radiation is the primary controlling factor in determining temperature (Gierasch and Goody 1968), advection and turbulent mixing may play a significant role. To our knowledge this feature is not present in the radio occultation profiles in this area, but the resolution of the Radio Science data near the ground and the time of observation (∼0400 local) are not ideal for identification of this feature.

Concomitant with the development of the two-layer inversion is the growth of a strong southwesterly low-level jet (Fig. 7b). Peak winds are near 18 m/s. It is not clear at this time whether the development of the jet is dynamically linked with the thermodynamic profile in the inversion. Blumsack *et al.* (1973), Ye *et al.* (1990), and Savijärvi and Siili (1993) found a similar low-level jet in simulations of slope flows on Mars.

One of the most striking results from the simulation is the large spatial variability of afternoon temperatures in the modeling


FIG. 7. Model vertical profiles of temperature (a) and wind speed (b) at the MPF landing site for various times during the last sol of the simulation. Profiles are as expected except for the development of the two-layer inversion several hours prior to sunrise. Height scale is approximate, because it is a function of time-dependent pressure values.
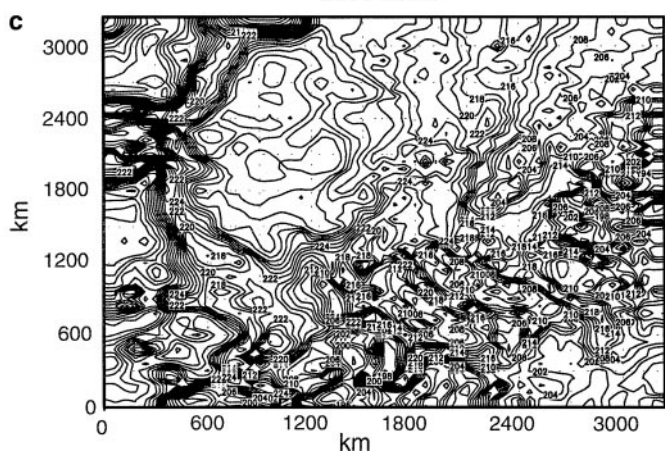
TEMPERATURE

0530 Local
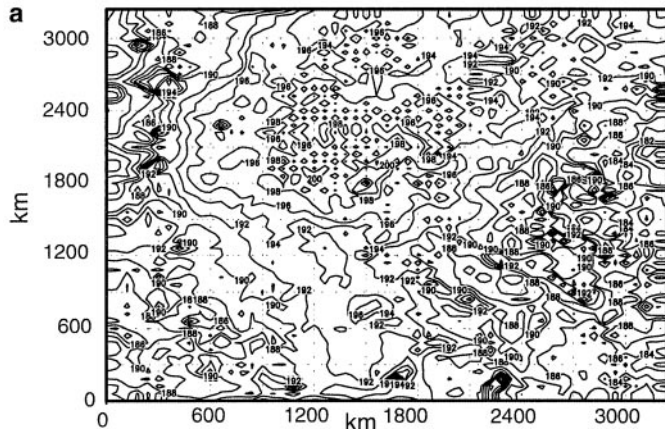
1530 Local
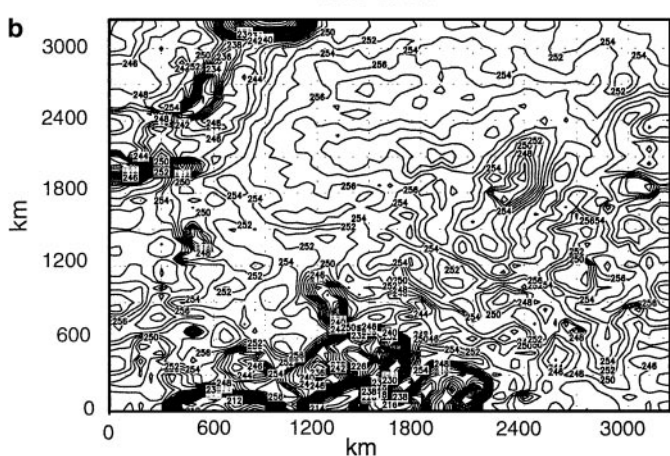
2030 Local

FIG. 8. Surface temperature during the last sol of the MPF landing site simulation at t = 0530 (a), t = 1530 (b), t = 2130 (c). Surface temperature is remarkably variable during the afternoon. Some 2 Δx noise is evident in the stable nighttime air as discussed in the text.

domain (Figs. 8a–8c). The variability is partly a result of variations in thermal inertia. However, a second and important effect is that of topography. Regions with relatively flat topography, such as the area immediately north of the MPFLS, tend to have relatively homogeneous temperatures. Areas of complex topography have the most variability. This result is somewhat unexpected, because radiation flux convergence is the dominant heating term and is roughly independent of moderate changes in elevation. Clearly, according to MRAMS, a one-dimensional model of equilibrium temperature has questionable validity in complex topography; advection (horizontal and vertical) of heat may be playing a significant role in the energy budget. Unfortunately, the limited *in situ* temperature measurements that are available are all in regions of relatively flat terrain. The processes that are producing the variability are still unknown, but efforts are underway to determine the root cause. We do not rule out the possibility of numerical error in these regions of complex and steep topography. Hopefully, future Mars missions will provide greater insight into the behavior of temperature in regions of complex terrain.

The modeled wind field is driven primarily by thermal forcing (Figs. 9a–9c), although topographic channeling is evident. Prior to sunrise, the winds blow downslope (Fig. 9a). During the day, winds blow upslope (Fig. 9b). The most noticeable example of upslope flow is in the southwest corner of the model domain in the direction of Tharsis. Peak winds are on the order of 20 m/s. There is also a noticeable south wind blowing from the canyon lowlands immediately south of the MPFLS. Peak winds in this area are also on the order of 20 m/s. The MPFLS is under the influence of weaker (10 m/s) winds blowing towards the highlands located to the east.

Once the sun sets (2130 local) the wind field quickly reverses. Strong katabatic winds develop and blow towards lower topography. Figure 9c captures the flow field at about the time of this wind reversal. Upslope flow is still evident in the Tharsis region in the very southwest corner of the domain, but farther down the slope the wind is weak and blowing downslope. The highlands to the east of the MPFLS already have a moderate katabatic wind flow pattern. By morning (0530 local) the katabatic downslope winds are reestablished and well developed (Fig. 9a).

The MPFLS is, coincidentally, in a position where many of the mesoscale topographic flows intersect and interact. One possible explanation for the small nocturnal temperature variations is the passage of mesoscale fronts associated with air masses originating from higher topography to the east and west.

B. Two-Dimensional Mountain Waves and Thermal Circulations

1. Background

Gravity waves are ubiquitous wherever wind encounters topography in a stable atmosphere. Under certain conditions, the waves may become highly amplified and nonlinear. On Earth,

WIND AND TOPOGRAPHY
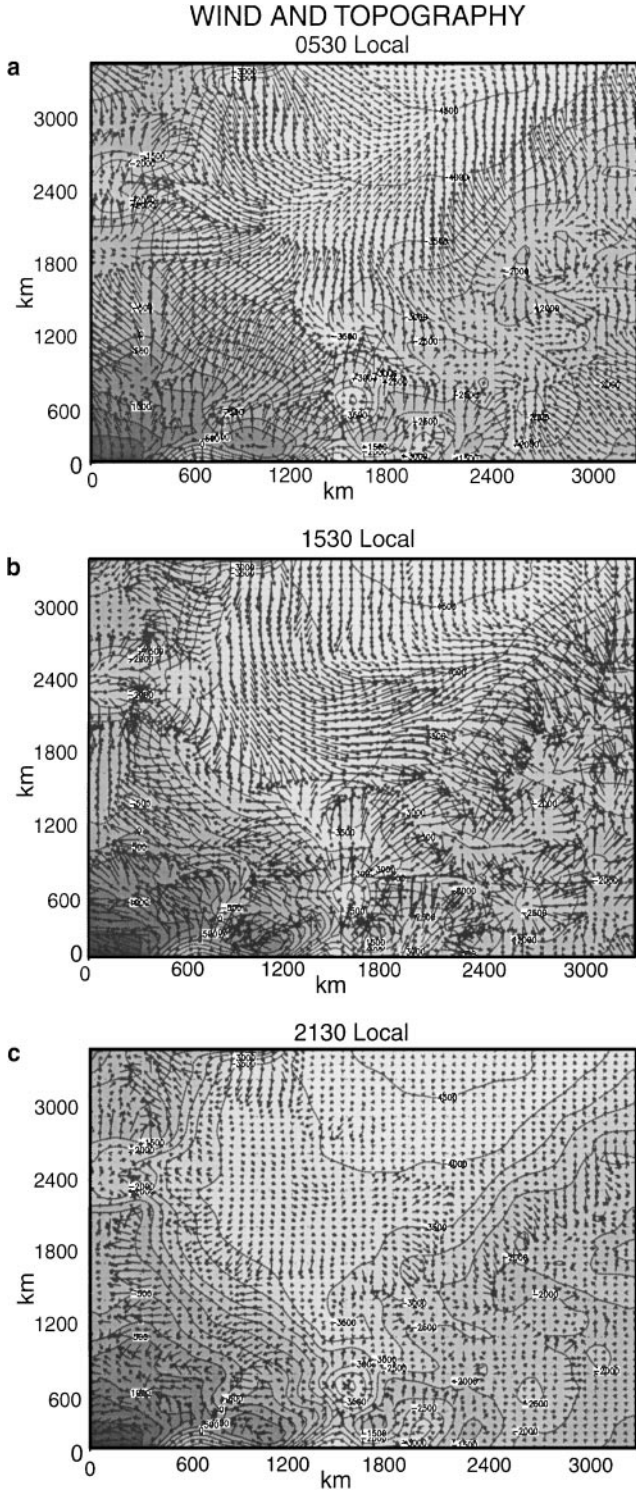
FIG. 9. Same as Fig. 8, but for wind vectors and underlying topography (shaded).

large amplitude gravity waves are often associated with downslope windstorms. Linear theory of stationary, small amplitude flow over two-dimensional or infinitely long barriers with simple and smooth topography on Earth is fairly well understood (the

"mountain wave problem"). An excellent treatment of mountain wave dynamics can be found in Durran (1986). Magalhães and Young (1995) obtained analytical solutions of the "mountain wave problem" subject to idealized martian atmospheric characteristics and suggested that these waves may also produce strong winds on and near the surface of Mars.

Linear theory demonstrates that the vertical structure of a mountain-induced stationary gravity wave is a function of the Scorer parameter, l, which is defined as

$$l^2 = \frac{N^2}{U^2} - \frac{1}{U}\frac{d^2U}{dz^2}. \tag{35}$$

N^2 is the static stability (Brünt–Väisälä frequency) and U is the mean horizontal wind speed. If the topography is decomposed into spectral components, then the vertical structure of the waves forced by the wave number k of the topography in a homogeneous (one-layer) atmosphere is given by

$$\hat{w}_i(z) = \begin{cases} A_i e^{\mu z} + B_i e^{-\mu z} & k > l \\ A_i' \cos mz + B_i' \sin mz & k < l \end{cases}, \tag{36}$$

where $\mu^2 = -m^2 = k^2 - l^2$, and m is the vertical wave number. When $k > l$ the wave amplitude decreases or increases exponentially with height. In a one-layer atmosphere the growing solution is eliminated by physical considerations. If $k < l$, then the structure is oscillatory with no loss in amplitude. The two regimes are referred to as evanescent (or external) and vertically propagating (or internal), respectively. For a fixed atmospheric structure (l), the characteristic wavelength of the ridge (k) determines the solution.

The generalization of the problem to a multilayer atmosphere requires the solution of a second-order differential equation with variable coefficients. The solution is difficult to obtain analytically. An indication of the effect, however, may be achieved by considering a two-layer atmosphere. In the lowest layer, waves may be internal or external and are permitted to amplify with height. In the second uppermost layer, the waves may be internal or external, but they may not amplify with height due to physical considerations. Additionally, waves propagating from the lower level can reflect off the interface between the two layers. Downward propagating waves can also reflect off the surface. Superposition of upward and downward propagating waves can produce trapped lee waves. Additional solutions are possible depending on how the Scorer parameter changes between the layers.

2. Numerical Experiment Design

A number of two-dimensional experiments are described, which demonstrate the behavior of flow impinging upon an idealized mountain barrier. The basic grid design is the same for all simulations: 500 m horizontal grid spacing and 15 m vertical

grid spacing at the lowest level stretched geometrically by a factor of 1.2 to a maximum of 1000 m for a total of 47 vertical points. The model top extends to approximately 20 km with the last few vertical layers acting as an absorbing layer to limit wave reflection off the model top. The horizontal domain is 200 grid points or 10 km. The time step varies from 2 to 5 s depending upon the simulation. A bell-shaped mountain given analytically by

$$h(x) = \frac{h_o a^2}{a^2 + x^2}, \tag{37}$$

where a is the half-width of the mountain is used as the lower boundary condition. The maximum height, h_o, is set equal to 1000 m in all simulations.

The atmosphere is initialized in two basic ways: (1) constant Scorer parameter with height (Type I simulation), and (2) atmosphere with diurnal variation (Type II simulation). The first type of initialization encompasses simulations designed for comparison with theoretical and analytical theory and without the complications of a variable and time-dependent Scorer parameter induced by radiative forcing. Three representative Type I simulations are presented that span the range of solutions.

The idealized Type I experiments demonstrate the ability of the model to produce results consistent with theory. Due to the short radiative time constant of the martian atmosphere, however, the lower atmosphere is anything but homogeneous and the static stability and winds may change dramatically over small time scales. The Type II simulation examines the dynamic response under a diurnally varying atmosphere. The Type II simulation is initialized with a presunrise profile, which is constructed by taking a sounding from the NASA Ames GCM grid point closest to the MPF landing site at $L_s = 140$.

a. Results. Table I displays the key parameters for the simulations presented in this section. The Type I experiments progress through the cases where $l > a^{-1}$ to $l \approx a^{-1}$ and finally to $l < a^{-1}$ for each of the idealized atmospheric initializations, which correspond to Experiments I-1, I-2, and I-3, respectively.

The Fourier spectrum of the topographical height is given by

$$F(h) = \frac{a h_o}{2} e^{-ka}, \tag{38}$$

TABLE I
Summary of Mountain Wave Simulations

| Experiment		N^2 (s^{-2})	U (m/s)	l (m^{-1})	$1/a$ (m^{-1})	Dominant solution
Type I	1	$1.e^{-4}$	10	10^{-3}	2.5×10^{-4}	Vertically propagating
	2	$1.e^{-5}$	10	3.1×10^{-4}	2.5×10^{-4}	Mixed
	3	$1.e^{-5}$	20	1.6×10^{-4}	3.3×10^{-4}	Damped
Type II	1	Varies in space and time	10	Varies in space and time	2.5×10^{-4}	Varies in space and time

where k is the wavenumber. According to (38), the mountain will force a continuous spectrum of waves, but the dominant waves correspond to the largest Fourier amplitudes, which e-fold at $k = a^{-1}$. Theory suggests the dominant solution can be found by comparing the Scorer parameter with a^{-1}. Figure 10 displays the horizontal and vertical wind speed for the Type I simulations. Note that the entire vertical domain is not displayed so that the structure near the surface can be more closely examined. Experiment I-1 exhibits a dominant vertically propagating wave with a vertical wavelength of about 4 km. Experiment I-2 also displays vertical propagation, but only the longest horizontal wavelengths exhibit this feature; the shorter horizontal wavelengths seen in I-1 are damped out. In Experiment I-3, nearly all waves are damped.

Consistent with observations on Earth, the greatest increase in horizontal wind speed relative to the background flow is observed with the large amplitude vertical propagating waves. The background wind speed is accelerated by approximately a factor of 2 in I-1. Also apparent in I-1 are turbulent rotor circulations in the lee of the mountain at the surface. Within the rotors, the vertical shear of the horizontal wind is very strong: approximately 0.025 s^{-1}. The vertical velocity is also greatest in I-1. Peak vertical velocity magnitudes are 2.5 m/s, and the vertical velocity circulations within the rotors are comparable to those associated with the mountain wave. There is little or no acceleration of the background wind in I-2 and I-3, and the vertical velocity perturbations are also much smaller in magnitude than those of I-1.

Focus is now given to the behavior of a more realistic martian atmosphere (Experiment II-1), which is achieved by activating the radiation parameterization absent in Experiments I-1 through I-3. The three-sol simulation exhibits flow regimes that are nearly repeatable from one sol to the next. We examine the last two sols of the three-sol simulation to eliminate concerns over model spin-up.

Prior to sunrise (0530 local) on the second sol (Fig. 11a), nearly laminar flow is found upstream of the mountain. In the lowest 500 m on the windward slope a shallow katabatic flow in excess of 6 m/s is present. This flow is in opposition to the 10 m/s west wind located directly above and is confined below the top of the nocturnal inversion. The result is an intense shear zone at the top of the inversion (approximately 500 m AGL). Even in this strong shear, the atmosphere is so stable that the flow remains nearly laminar. A 1–2 km deep west wind in excess of 22 m/s extends from the ridge top, along the lee slope, and over 40 km into the plains. This strong flow results from the juxtaposition of the downslope katabatic wind and the mountain-wave induced downslope wind. The strong shear zone present to the east of the ridge is not found on the leeward slope.

Directly over the mountain ridge at 5 to 6 km above the surface, the atmosphere becomes highly turbulent. Examination of the model spin-up phase (not shown) clearly shows that the origin of this turbulence is the breaking of internal gravity waves. For example, folding and overturning of the isotropic surfaces is evident. Once the waves break, a critical level (level of
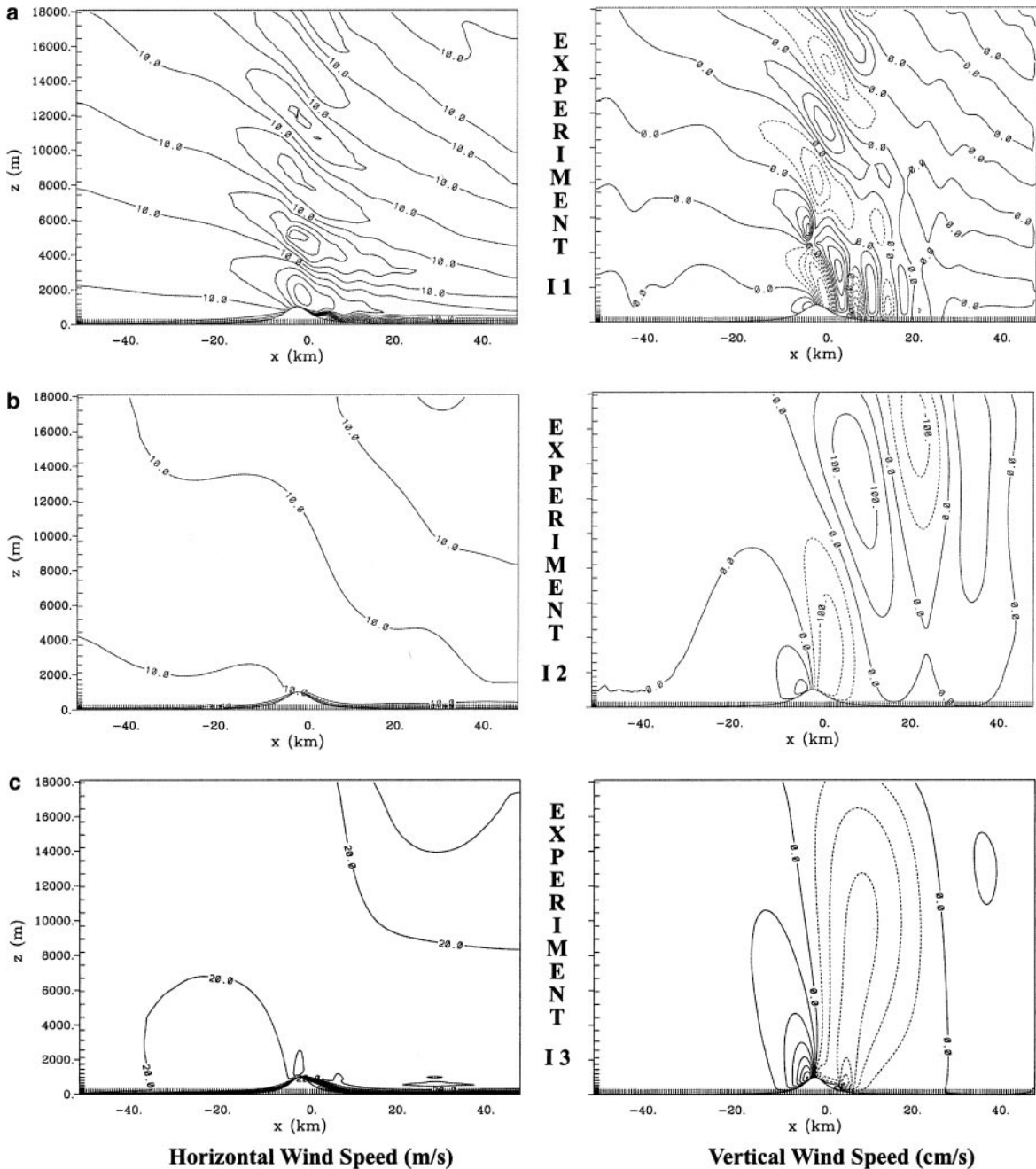
FIG. 10. Horizontal wind (left column) and vertical velocity (right column) for idealized mountain wave experiments I-1 through I-3. The entire vertical domain is not displayed so that details near the surface can be more easily discerned.

wind reversal) develops, which strongly limits the propagation of waves. This so-called self-induced critical level traps most of the wave energy below, which results in acceleration of the mean flow downstream of the mountain. In a linear model, the critical level would completely prevent vertical propagation of waves, but in MRAMS some wave energy leaks through, and the breaking waves can trigger waves that propagate to higher altitudes. Waves on the scale of the mountain are clearly evident in the temperature field above 14 km AGL (Fig. 11b).

Afternoon heating produces a drastically different scenario. At 1530 local time the wind (Fig. 12a) and temperature (Fig. 12b) fields exhibit highly turbulent circulations in the boundary layer. The boundary layer is more shallow on the wind-ward side (<4 km) and higher on the leeward side (~5 km). The strongest winds in the simulation are found at this time and are located at or very near the surface. Peak westerly winds are greater than 32 m/s and peak easterly winds are greater than 18 m/s. The self-induced critical level is still present and lies
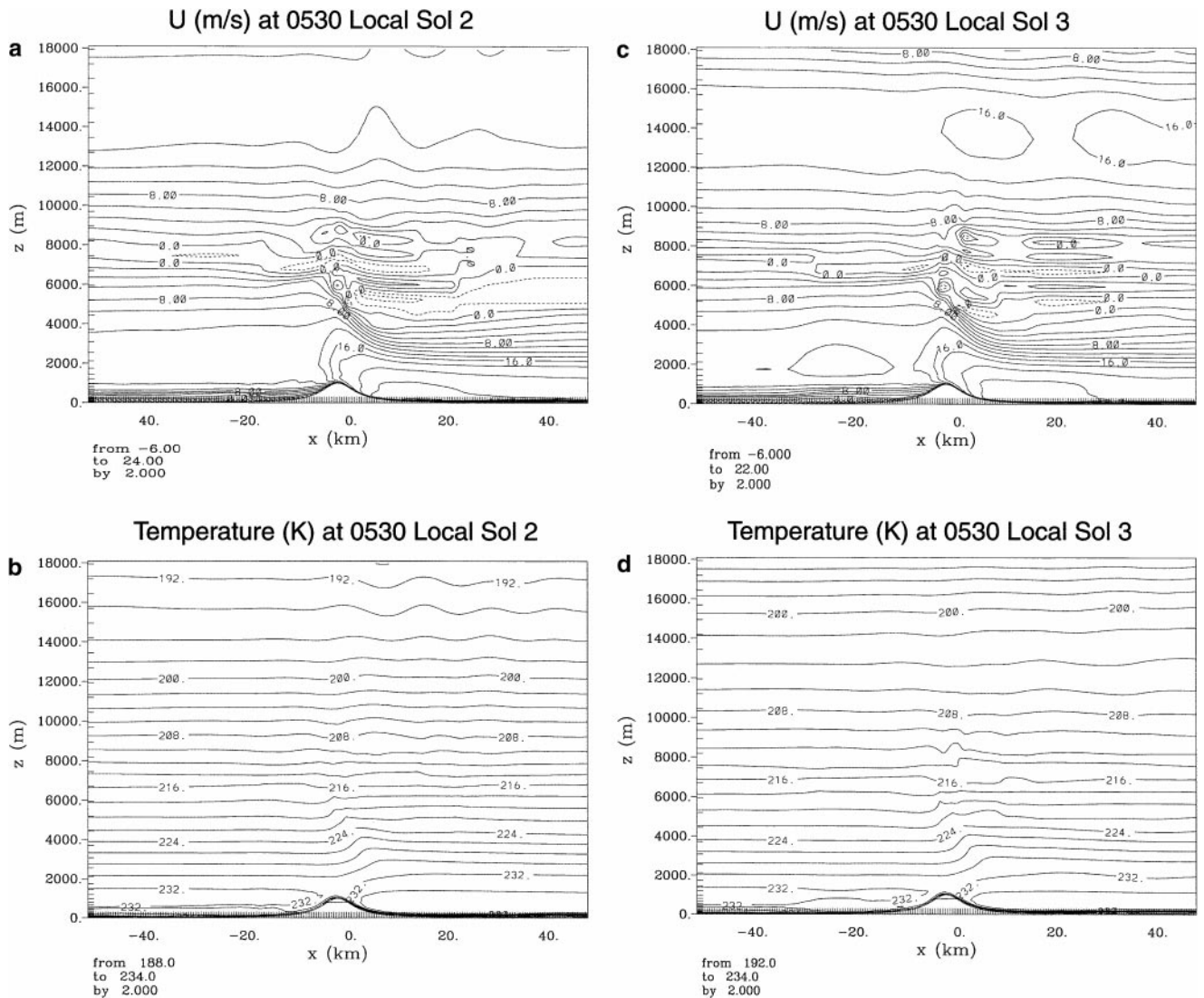
FIG. 11.   Horizontal wind and temperature at 0530 local on the second (a and b) and third sol (c and d) of experiment II-1. The entire vertical domain is not displayed so that details near the surface can be more easily discerned.

over the convective boundary layer. High-amplitude wave activity is seen directly above the critical level. This activity underlies a deep (14 to 17 km AGL) westerly wind on the order of 16 m/s. Most of the turbulence in the boundary layer is convectively generated, but the increase in depth and intensity of the boundary layer circulations to the lee of the mountain clearly indicate that wave energy is being deposited in the boundary layer. The most striking features in the temperature field are convective plumes rising from the surface. Wave activity is evident above the convective boundary layer.

Within a few hours after sunset (2130 local), the convective plumes have subsided and the atmosphere quickly returns to a state that closely resembles the early morning state (Figs. 13a and 13b). Downslope katabatic winds are developing, the strong surface winds in the lee of the mountain have developed, and the critical level is well defined.

In each of Figs. 11 through 13, we have shown the state of the atmosphere exactly on sol later. The purpose is to demonstrate that the flow features are highly repeatable from day to day.

The results from the II-1 Experiment indicate that the diurnal variation of stability has the greatest influence near the surface. However, the characteristics of the vertically propagating waves are also modified. The strongest sustained winds are found far in the lee of the barrier during the strong heating of the afternoon. These winds are associated with highly turbulent circulations and are most likely very gusty in nature. During the day, the strongest winds are not restricted to the lee of the barrier and are often on the windward slope or near the mountain top. In the evening, the winds in the lee of the mountain remain strong but are less than those found in the afternoon. Additionally, the nighttime winds are more laminar (less turbulent). The vertical shear of the wind is extremely intense most of the time.
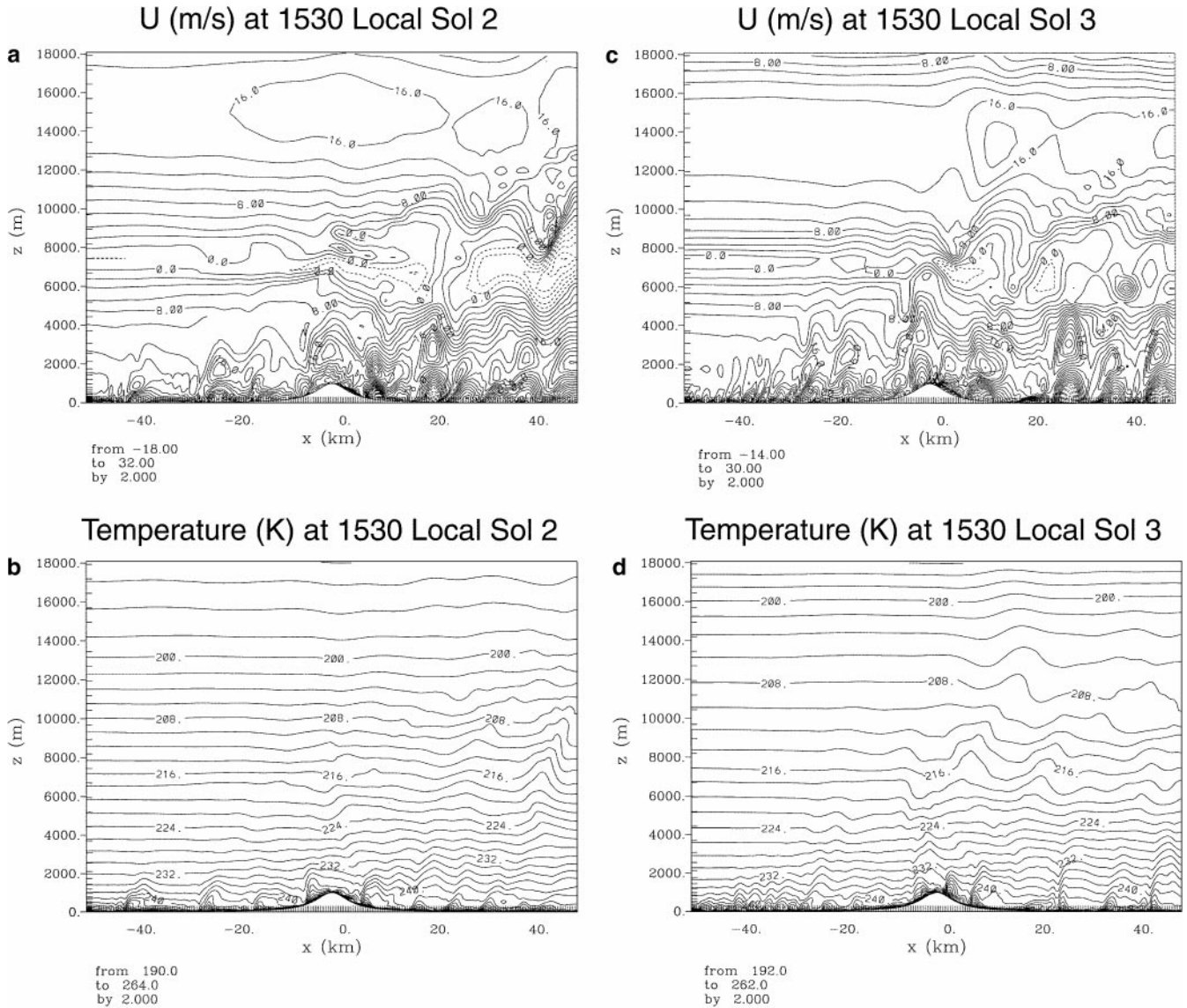
U (m/s) at 1530 Local Sol 2

a

from −18.00
to   32.00
by   2.000

U (m/s) at 1530 Local Sol 3

c

from −14.00
to   30.00
by   2.000

Temperature (K) at 1530 Local Sol 2

b

from 190.0
to   264.0
by   2.000

Temperature (K) at 1530 Local Sol 3

d

from 192.0
to   262.0
by   2.000

FIG. 12.   Same as Fig. 11, but at 1530 local.

The simulations indicate that regions of Mars with moderate topography are likely highly turbulent and prone to strong shear when moderate (10 m/s) mean winds are present. These findings, therefore, have clear implications for future missions involving near-surface (e.g., balloon or aircraft, lander, or human exploration).

Although we do not attempt to do so here, simulations that explicitly resolve mountain waves may be utilized to improve and validate the gravity wave drag parameterizations that are used in GCMs. It is rather straightforward, for example, to compute the pressure work term from the explicit simulation, and this result could be compared to a parameterized solution.

With respect to wind streaks, it appears that a 10 m/s wind blowing perpendicular to a mountain ridge of modest height (1 km) can result in significant leeward acceleration of the wind.

The most persistent winds are found at night, but the strongest winds are during the day. Thus, dust is more likely to be lofted during the day but may not generate a well-defined pattern on the surface as a result of the transient and turbulent circulations. The nighttime winds are less likely to entrain dust but would be more likely to generate a wind streak pattern. Any dust lifted during the night could be transported far downstream.

C. Large Eddy Simulations

1. Background

Large eddy simulations (LESs) are designed to explicitly model the large boundary layer eddies that transport heat and momentum. The grid spacing must be less than the eddies themselves, but the computational domain must be large enough to
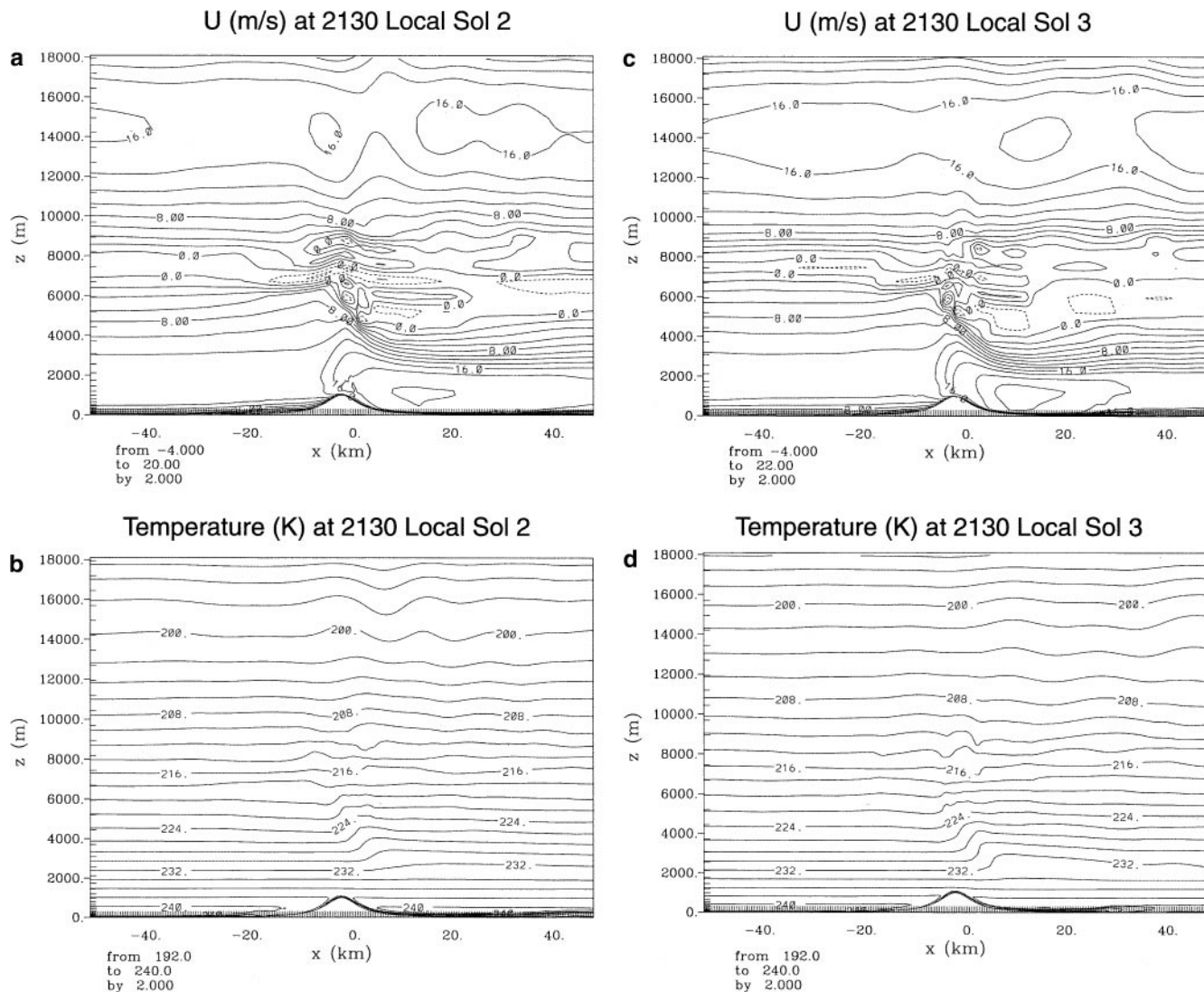
U (m/s) at 2130 Local Sol 2

U (m/s) at 2130 Local Sol 3

Temperature (K) at 2130 Local Sol 2

Temperature (K) at 2130 Local Sol 3

FIG. 13.   Same as Fig. 11, but at 2130 local.

contain a large enough sample of eddies so that meaningful ensemble statistics can be obtained from the results. In nearly all LESs, the boundary conditions are cyclic and the topography is flat and of uniform composition.

A reasonable estimate for the size of a boundary layer eddy is obtained from the boundary layer depth. Therefore, a typical eddy size is on the order of a few tens of meters to more than a kilometer. The time step associated with these scales ranges from tenths of seconds to a few seconds. As a result of the small grid spacing, small time steps, and the requirement for a relatively large domain, LESs are extremely expensive to undertake computationally.

The three-dimensional LES presented herein required approximately 36 hours of uninterrupted computer time for each hour of simulation; a full-sol simulation would require over one month of uninterrupted CPU time using a SUN ULTRA 60 with 512 Mbyte of memory. The storage space required to store the output from a one-sol simulation is on the order of 20 Gbyte. Due to these computational restraints, only the first half of a sol has currently been investigated.

Since a LES of Mars has never been published in the literature, it was unclear exactly how to optimally configure the simulations. Testing LES model configurations in three dimensions is an extremely slow and tedious process. Consequently, two-dimensional LESs were conducted first to provide guidance for the full three-dimensional simulation. The major disadvantage of a two-dimensional simulation is that vorticity stretching cannot operate, and it is this process which drives the small-scale circulations to even smaller scales.

Based on the results of the 2-D LES, the computational domain of a 3-D LES was constructed as follows: 100 m grid spacing covering a domain of 18×18 km with cyclic boundary conditions. Vertical grid spacing started at 12 m at the surface and was gradually stretched up to a maximum of 250 m at a height

of approximately 9 km. This configuration is not the ideal LES configuration, but it was constrained by memory and processor speed. The 3-D simulation was initialized with a representative presunrise (0530 local) thermodynamic sounding taken from the 2-D LES. A backing wind profile with wind speed increasing with height was used to initialize the kinematics. A backing wind turns clockwise with height.

The first few hours of the 3-D simulation may be regarded as "spin-up," or can be viewed as the response of a nonturbulent and horizontally homogeneous atmosphere to radiative forcing. We believe that the high stability of the nighttime martian atmosphere damps turbulent motions so strongly that the initial homogeneous conditions are a reasonable approximation to the atmospheric state that would be found over a homogeneous martian surface. After the "spinup," the simulated atmosphere becomes sufficiently turbulent, and the homogeneity of the initial atmosphere is inconsequential.

2. LES Results

At the onset of heating, the atmosphere quickly organizes into weak rolls aligned perpendicular to the wind (Fig. 14a). These circulations persist for approximately 4 h into the simulation, during which time the depth of the circulations increases from a few hundred meters to over 2 km. The average horizontal wavelength of the rolls is approximately 2 to 3 km. If these circulations were visible as clouds, they might appear as cloud streets with regularly spaced cloud elements. The vertical velocity within the rolls is less than 0.5 m/s, and is closer to 1 cm/s early in the simulation. The rolls appear to be primarily mechanically driven, and appear dynamically similar to those found on Earth (Hadfield *et al.* 1991). As solar heating progresses, the strong radiation inversion is eroded, and the decreased stability (and Richardson number) permits the shear to produce deeper and stronger overturning circulations.

Mechanically driven circulations transition to buoyancy-driven circulations between 3 and 5 h after sunrise. The width of the ascending branches of the rolls narrows to less than 0.5 km and the vertical velocity increases to over 5 m/s (Fig. 14b). Local maxima in updraft and downdraft strength also become increasingly pronounced. These signal the presence of buoyant updraft plumes focused within the rolls. The depth of the boundary layer increases concomitant with the enhanced convection. Mesoscale organization of the updrafts is present, but the well-defined shear vector alignment that was present earlier in the simulation is not as obvious.

After 5 h into the simulation, the boundary layer turbulence is strongly forced by buoyancy (Fig. 14c). Deep convective plumes emerge from the surface and quickly penetrate to altitudes of 3 to 4 km. As the plumes ascend, downward return circulations develop along the outer edge of the rising air. Also, the width of the plumes increases with height. Occasionally, a plume may detach from the surface and evolve into a rising thermal. The scenario is not unlike the spectacle observed

in a lava lamp. A cross section at 7.5 hours into the simulation reveals plumes beginning their ascent, plumes beginning to detach from the surface, and thermals that were once plumes (Fig. 14d).

The behavior of the convective thermals and plumes is consistent with terrestrial observations of the convective boundary layer, which show that areas of upward motion are stronger and narrower than the downdrafts (Mason 1989). Numerical simulation results presented by Mason (1989) and Schmidt and Schumann (1989) strongly resemble those presented here. The most notable similarities are the elongated and narrow updrafts and the deep, penetrating convective plumes.

Turbulent statistics clearly identify the onset of convection and the growth of the boundary layer (Fig. 15). Domain-averaged instantaneous values in Fig. 15 are produced by horizontally averaging quantities to generate mean fields for each model layer. The average field is then subtracted from the total to produce a perturbation. Correlations and covariances are then obtained by multiplying the perturbation fields and averaging for each horizontal layer.

The covariance of vertical velocity and temperature (Fig 15a) is rather large compared to typical Earth values, which are roughly an order of magnitude smaller. For example, during the Pheonix II boundary layer study, typical maximum values were on the order of 0.2 Kms^{-1} (Schneider 1991). The Phoenix II experiment was conducted in the Arizona desert near the summer solstice and is perhaps as close to the martian environment as one can get while on Earth. Owing to martian air density roughly two orders of magnitude smaller than on Earth, the actual energy flux, which is obtained by multiplying the covariance by density and heat capacity, is about one order of magnitude smaller than on Earth. This leads to the interpretation that the martian daytime boundary layer is extremely vigorous with intense updrafts and downdrafts correlated with hot and cool air, but it is also rather inefficient in transporting energy due to the low density.

The modeled heat flux values are of the correct order of magnitude when compared with previous studies of the martian boundary layer. Haberle *et al.* (1993a) indicate peak surface heat fluxes of about 27 W/m^{-2} and 12 W/m^{-2} for the Viking Lander 1 and Viking Lander 2 sites, respectively, for a surface roughness length of 1.0 cm. The heat fluxes were roughly halved for a roughness length of 0.1 cm.

Turbulent kinetic energy (Fig. 15b) and vertical velocity variance (Fig. 15c) bear out the interpretation of the vigorous convective boundary layer. These values are roughly two to three times the typical values on Earth (Schneider 1991). Vertical velocity variance contributes to roughly half the turbulent kinetic energy, which indicates that the turbulence is not isotropic.

One of the more interesting and somewhat unexpected results is the positive and negative vertical flux of horizontal momentum (Fig. 15d), which indicates periods of gradient and counter-gradient momentum transport. The cause and significance of this is not clear at this time and warrants further investigation.
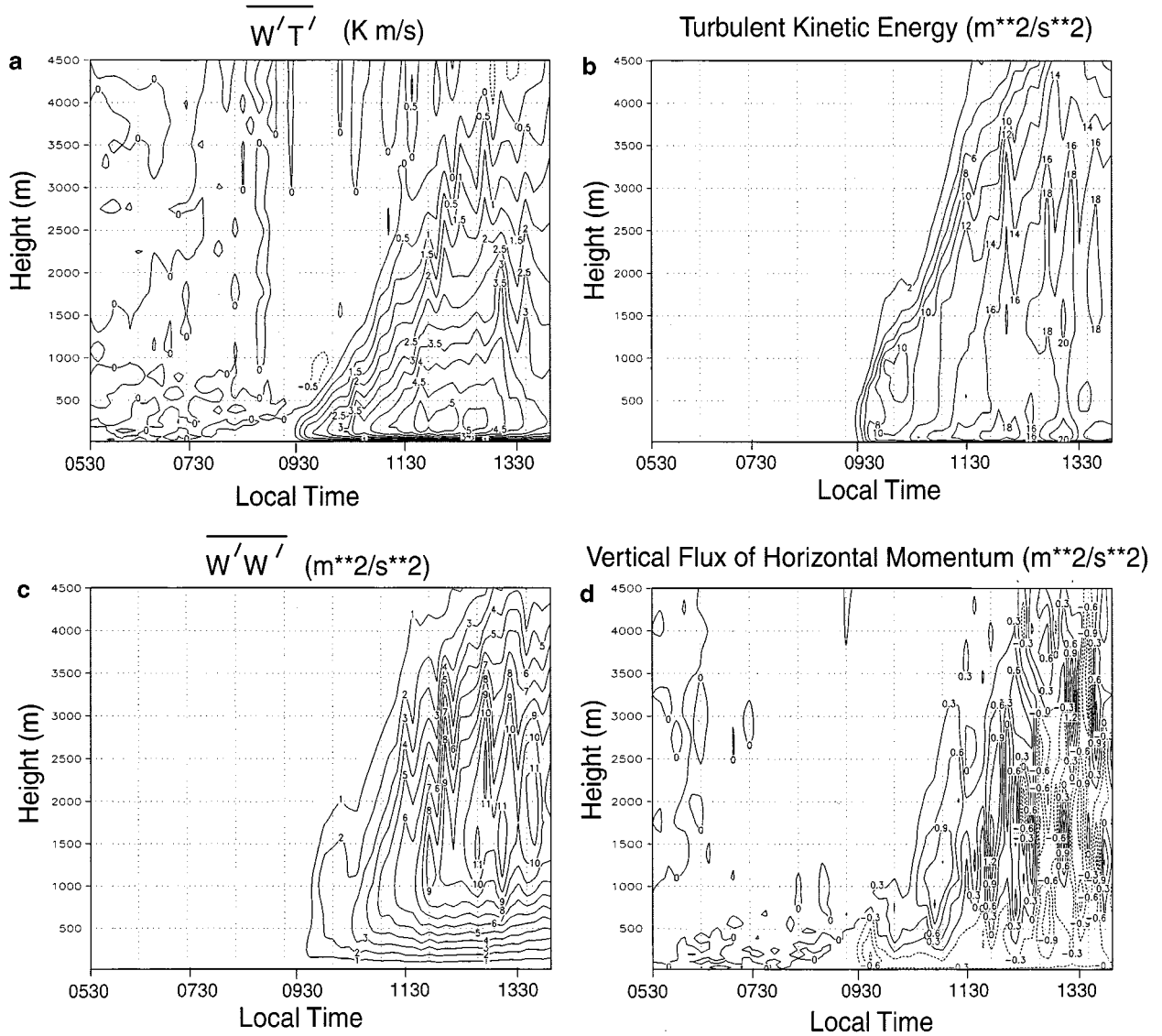
Vertical Velocity (m/s)
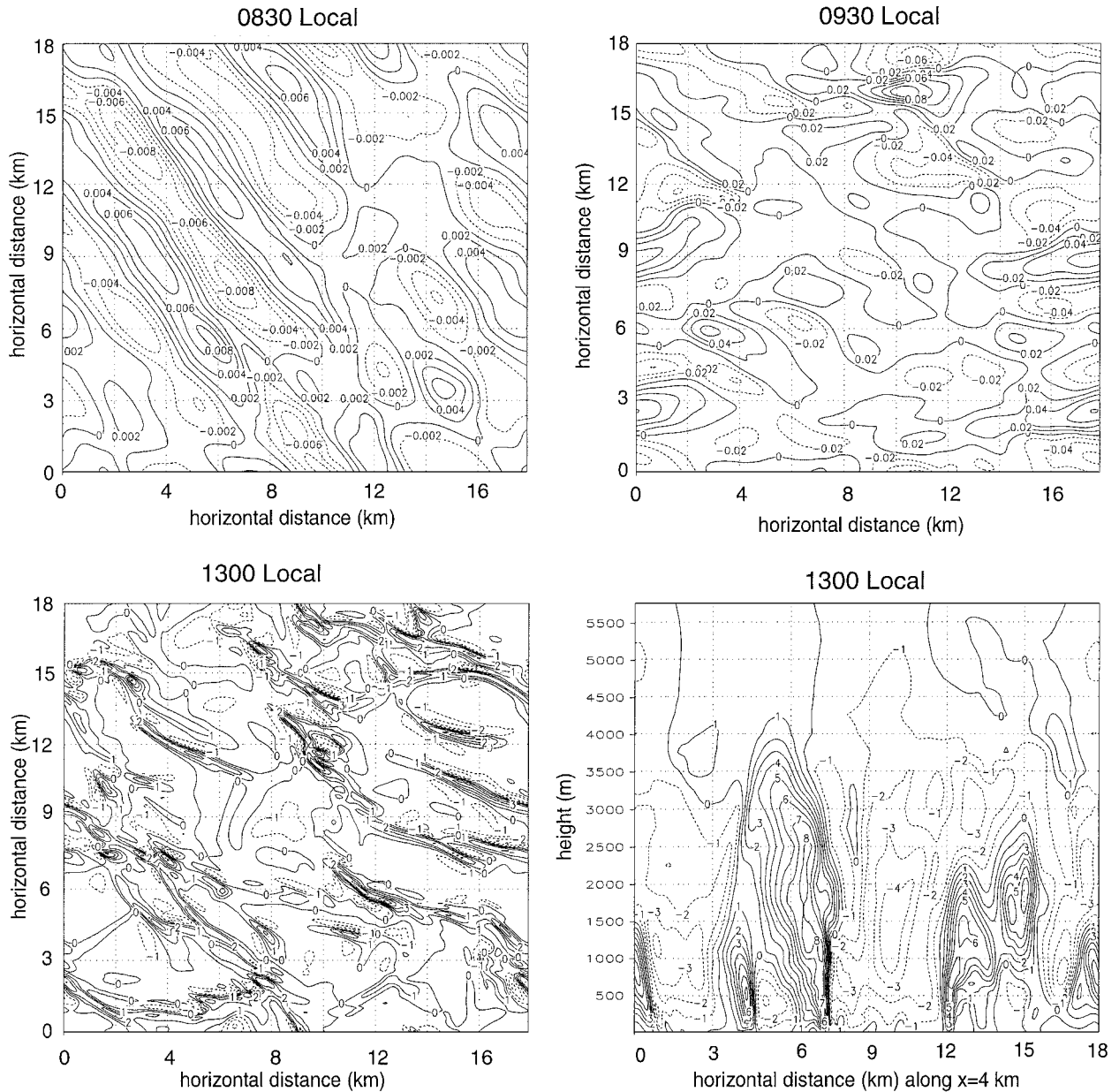
FIG. 14. Vertical velocity (m/s) from the large eddy simulation. Horizontal cross section at $\sim z = 150$ m at 0830 (a), 0930 (b), and 1300 (c). A vertical cross section through x = 4 km at 1300 (d). Only a portion of the domain is shown so that the circulations of interest can be identified.

Dust devils appear to be ubiquitous across large plains during the daytime on Mars (Ryan and Lucich 1983, Thomas and Gierasch 1985, Metzger *et al.* 1999). A LES should in principle be able to capture these features. The motivation for initialization of the model with a backing wind profile was to provide a source of environmental vorticity that might aid in the development of these features, although the contribution of environment shear vorticity to dust devils is strictly speculative.

The model output was examined every ten minutes for indications of dust-devil-like circulations. Observations of terres-

trial dust devils indicate that the circulations are nearly in cyclostrophic balance with the low pressure core (Sinclair 1966). Many regions of locally maximized vorticity and locally reduced pressure were discovered in the model output, but only during the mid- and late-afternoon hours. Figure 16 displays relevant fields for one such case. Note that the entire horizontal domain is not displayed. To elucidate the circulation, the mean wind has been subtracted from the total field to yield perturbation winds in constructing the wind vectors shown in Fig. 16. There are two vortices of interest. At z = 12 m (Fig. 16a), an anticyclonic

Large Eddy Simulation Turbulence Statistics

FIG. 15. Turbulent statistics derived from the large eddy simulation. Heat flux (a), vertical flux of horizontal momentum (b), turbulent kinetic energy (c), vertical velocity variance (d).

circulation is centered at (9.2, 8.6), and a more disorganized circulation and shear line is located near (7.5, 9.3). At $z = 380$ m (Fig. 16b), the first anticyclonic circulation is still clearly evident and much larger in area. The second circulation is expressed as two counter-rotating vortices at $z = 380$ m. Wind speeds around the circulations are in excess of 20 m/s (Fig. 16c). A vertical cross section at $y = 8.3$ km through the first circulation demonstrates that it has a well-defined updraft core of approximately 10 m/s extending to a height of roughly 1.5 km (Fig. 16d). A strong gradient of wind speed surrounds the core at low levels and gradually relaxes with height. Figure 17a displays the pressure and vertical velocity at $z = 12$ m along an east-west line intersecting the anticyclonic vortex, and the same is shown in

Fig. 17b at $z = 380$ m. The pressure perturbation is on the order of 1.0 Pa. Other areas within the model domain show similar pressure perturbations (up to ∼2 Pa) at various times during the afternoon.

At any given time, there appears to be from one to four of these disturbances within the domain, which gives an areal coverage ranging from 0.03 to 0.1 per km². It is unclear at this point in the research whether the modeled phenomena are true dust devils, but they do present similar characteristics. Metzger *et al.* (1999) discussed five dust devil plumes imaged during MPF. The observed dust devils ranged in size from approximately 14 to 80 m in diameter. These dimensions are smaller than the dimension of the modeled circulations, which are roughly
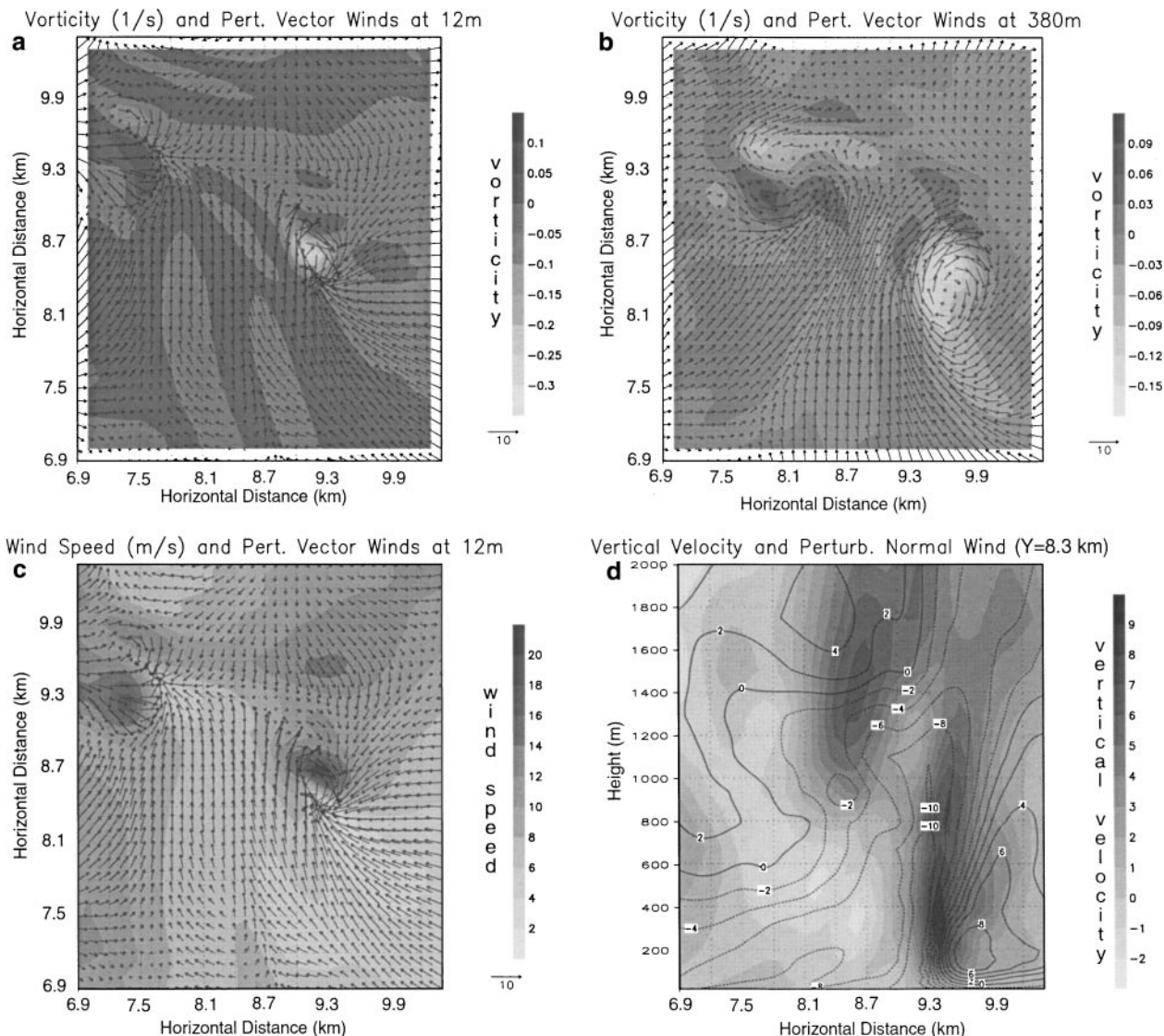
FIG. 16. Dust-devil-like circulations captured during the large eddy simulation. Vertical vorticity and perturbation vector winds at z = 12 m over a portion of the model domain (a). Vertical vorticity and perturbation vector winds at z = 380 m over a portion of the model domain (b). Wind speed and perturbation vector winds at z = 12 m (c). A cross section along y = 8.3 km displaying vertical velocity (m/s; shaded) and meridional wind (m/s in and out of the page (contours) (d). Only a portion of the domain is shown so that the circulations of interest can be identified.

five times larger. However, the observed dimensions are based upon the visible portion of the dust devil; the circulation likely extends beyond the dust-laden area. The height of the modeled circulations appears to be taller than the observed dust devils.

Schofield *et al.* (1997) analyzed the passage of a low-pressure perturbation that was correlated with a wind shift and suggested the signature was that of a dust devil. Unfortunately, wind speed was not available. The observations are not inconsistent with the modeled low-pressure perturbations and associated circulation. The highest modeled low-pressure perturbations were on the order of 2 Pa, which is similar to the roughly 3-Pa observed departure.

Future numerical studies will examine these circulations in more detail by nesting to higher resolution and increasing the output frequency of the model to better capture the life-cycle.

D. Big Crater Simulation

The Mars regional atmospheric modeling system was used to investigate the complex nature of topographically forced circulations and atmosphere–surface interactions generated by atmospheric flow over a crater similar to Big Crater, which is located near the MPF landing site. The model atmosphere was initialized in the following manner. A horizontally homogeneous
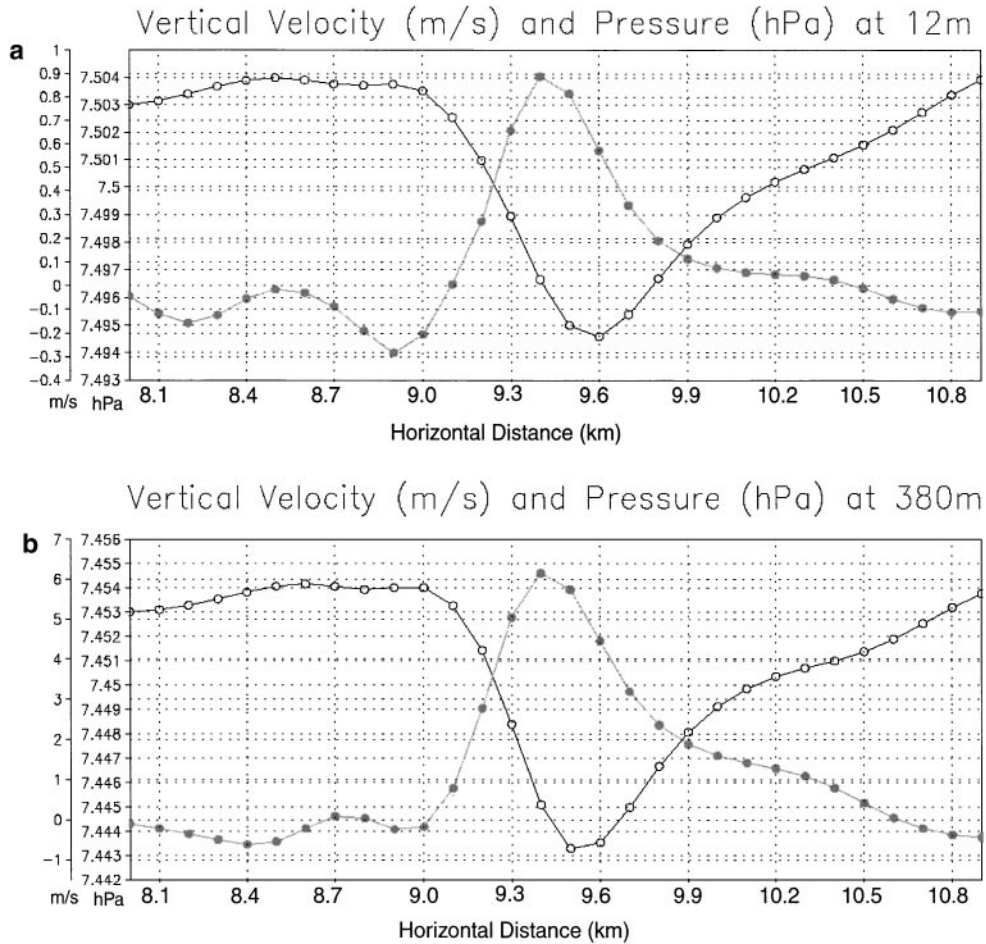
FIG. 17. Trace of pressure (○) and vertical velocity (●) along the z = 12 m and z = 380 m surface and slicing through the core of the dust devil in Fig. 16. The modeled pressure perturbation is similar to the one observed during the passage of a dust devil in the ASI/MET experiment.

temperature profile with a uniform stability of 1.0×10^{-4} s^{-1} was used to initialize a two-dimensional simulation over a flat surface. The model was then run for two sols beginning and ending at 0530 local time. The location of the modeling domain was that of the MPF landing site, and orbital geometry corresponds to approximately $L_s = 142$. After integrating for two sols, the simulated atmosphere produced a reasonable looking boundary layer profile and exhibited a reasonable diurnal variation during the second sol. The atmospheric profile from the two-dimensional simulation was used to initialize the three-dimensional crater simulation (Fig. 18). The initial wind profile is a uniform westerly wind of 10 m/s at all levels.

The surface topography for the crater simulation is constructed by processing a two-dimensional crater profile, which was supplied by R. Kuzmin (personal communication, 2000) and obtained from the Mars orbiting laser altimeter. The raw profile is roughly 3 km from rim to rim. The raw crater profile is scaled to a 1-km rim-to-rim crater similar to Big Crater, in the following manner:

1. The raw crater size (diameter) is obtained by finding the distance from the minimum to the maximum topographical height and doubling the value.

2. The raw data (both height and distance) are then scaled by the same factor so that the scaled data produce a crater diameter of exactly 1 km. Since the raw data reveal a crater near 3 km, the scaling factor is roughly 1/3.

3. The average topography height is calculated and subtracted from the data to produce a perturbation height field.

4. Only the right-hand side of the crater, defined from the minimum (center) data point of the crater and onward, is used to construct the three-dimensional topography; the first half of the data is neglected.

5. The last (far from the crater) two data points are less than 2 m and are set to 0 m. 3-D model topography is given a perturbation height value obtained by linear interpolation from the 2-D crater profile of height versus distance (Fig. 19).

The resulting crater topography produces a crater similar in size and dimension to that of Big Crater. It is not, of course, the
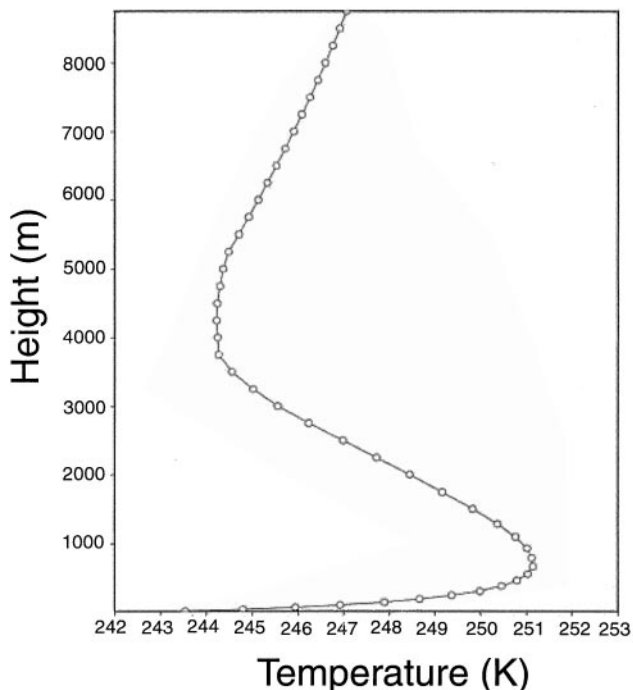
Initial Atmospheric Temperature Profile

FIG. 18.   Initial temperature profile used to initialize the crater simulation.

same as Big Crater. However, since Big Crater seems to be fairly representative of other craters of comparable size, we believe that the circulations that result from the model topography will not differ substantially from that which would be produced by Big Crater.

The model domain is covered by two, two-way nested computational grids. The first grid is 40×40 points in the horizontal with a grid spacing of 500 m and 47 points in the vertical with the lowest level at 12 m above the surface. The vertical grid spacing is gradually stretched with height to a maximum spacing of 250 m. The total height of the domain is approximately 9 km. The second grid is 102×67 points in the horizontal with a grid spacing of 100 m. The vertical grid spacing of the second grid is the same as the first. The second grid is centered on the crater and nested within the coarser first grid. The model run was started before sunrise (0530 local) at the MPF site at $L_s = 142$.

Prior to the development of a highly unstable convective boundary layer, the atmosphere flow is nearly laminar as it flows around the crater. The highly stable nocturnal inversion requires most of the impinging air to flow around the topographic obstacle. Surface friction reduces the low-level wind speeds. The crater rims are exposed to wind speeds higher than the surrounding surfaces due to their exposure. The greatest surface stress is found on the downwind crater rim (Fig. 20a). A broad region of higher surface stress is also found in the lee of the crater. The maximum predicted friction velocities are on the order of

0.5 m/s with a 5-cm roughness length and 10 m/s free stream wind velocity.

A few hours after sunrise, the depth of the unstable convective boundary layer grows to several kilometers and the atmosphere within this layer becomes highly turbulent (Fig. 20b). The adiabatic and superadiabatic atmosphere feels no downward-directed buoyancy-driven restoring force, and the air is free to flow over rather than around the crater. Superimposed on the crater circulation are boundary layer convective rolls aligned parallel to the mean atmospheric shear vector. The juxtaposition of the crater and convective circulations produces a non-steady turbulent region in the lee of the crater, which sweeps out a wedge-shaped area in the lee of the crater (Figs. 20c and 20d). The maximum surface stress gradually increases to a value slightly in excess of 1.0 m/s. Maximum values are again found on the downwind rim of the crater and occasionally in the turbulent region downwind of the crater. The leeward rim experiences moderate to high stress values that are typically less than those on the downwind rim.

The predicted wind stress patterns are consistent with wind streak patterns observed in the lee of small craters, hills, and ridges. The higher stress on the downwind crater rim is also consistent with the MOC image interpretation of many small crater rims, which show preferentially higher erosion on the downwind rim (R. Greeley, personal communication, 2000).

The simulation was terminated approximately 12 h into the numerical integration. Future modeling work will examine the
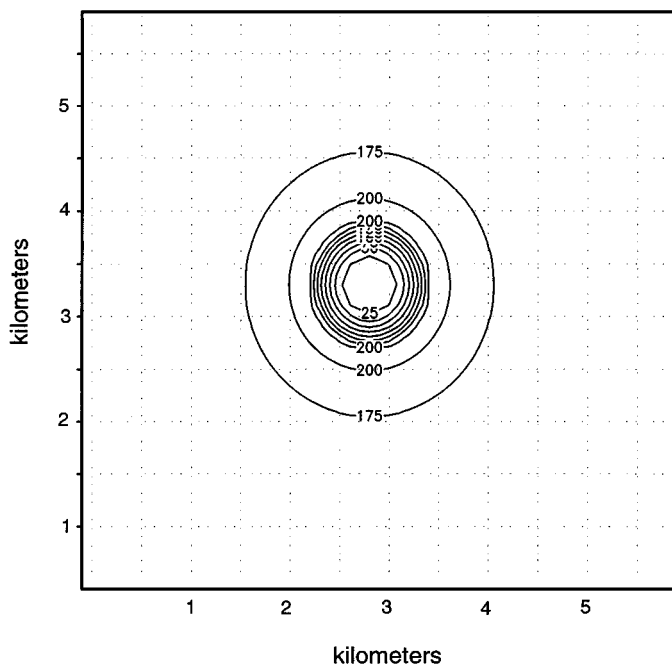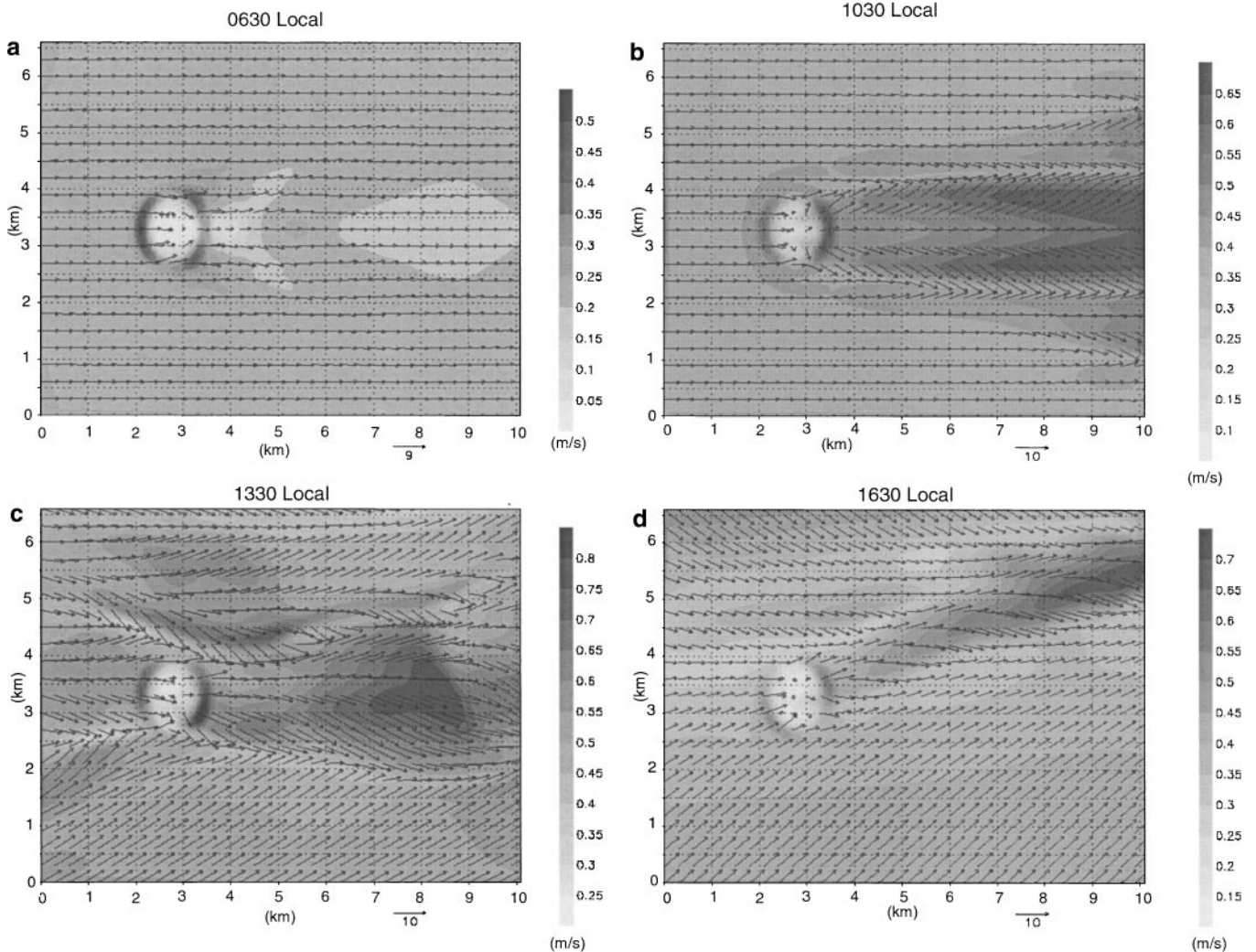
Crater Topography (m)

FIG. 19.   Crater topography. Only a subset of the modeling domain is displayed.

Friction Velocity (shaded) and Wind (vectors)

FIG. 20. Friction velocity and wind vectors for selected times (as indicated) from the crater simulation. Enhanced regions of surface stress correlate well with observed erosion on crater rims and with dust streaks in the lee of the crater.

atmosphere–surface interaction as the sun sets and the nocturnal inversion redevelops.

IV. CONCLUSION

The Mars regional atmospheric modeling system is a new tool that can be used to investigate the complex physics of regional, mesoscale, and microscale atmospheric phenomena on Mars. MRAMS is adapted from a widely used terrestrial model. Modifications for applicability to Mars include the addition of the NASA Ames GCM radiation code, a new formulation for the processing of gridded data for use as initial and boundary conditions, and the ability to ingest gridded surface properties.

MRAMS was applied under a wide range of scenarios that include simulation of the Mars Pathfinder landing site, a large

eddy simulation of the convective boundary layer, investigation of mountain waves and thermally induced slope flows, and the simulation of flow over an idealized Big Crater.

The results at the landing site were shown to be in very good agreement with observations. The maximum temperatures were slightly underpredicted, which may have been caused by uncertainties in surface thermal properties but may also result from the extrapolation of the temperature to the height of the observation instrument. Wind direction showed good agreement with observations, particularly in the afternoon. The model failed to produce winds that fully rotated through all compass directions. Modeled wind directions two grid points to the south of the landing site did reveal a full rotation, which suggests that a higher resolution simulation that better captures the topographic detail of the area may provide better agreement. Additionally, the

modeled wind speeds were generally less than observed. The quality of the observations, however, is not well known, and it may be that the observational values are too large.

At least a few interesting, new, or unexpected findings resulted from the MPF landing simulation. First, there was surprising horizontal variability in the near-surface temperatures. This was particularly true in the afternoon and in regions with steep topography. A portion of the variability can be explained by variations in thermal inertia, but the atmospheric circulations in and around the topographic features also seemed to play an important role. We also have not yet ruled out the possibility of numerical instability along the steep slopes. Such instability is known to exist in sigma-z coordinate models when applied to very steep slopes, especially when strong vertical gradients of atmospheric properties are present. Second, the model showed the development of a nearly isothermal layer during the early morning hours. The development of this feature has not been identified in previous studies. It is not clear why the isothermal layer develops, but it is clearly not a radiative response. This topic is left for future study.

A numerical dilemma surrounding the turbulent diffusion parameterization was identified. Owing to the highly stable nocturnal inversion, the modeled diffusion was of insufficient strength to damp nonphysical model solutions. Artificially increasing the diffusion tended to alleviate the problem but simultaneously increased the disparity between observed and modeled temperature. This problem was also left open for future research.

Finally, the diurnal pressure cycle was captured by the model, but the amplitude was smaller than observed and the tidal signatures were absent. It was not expected that MRAMS would produce a tide since the model is regional rather than global. However, it was hoped that the boundary conditions, which were supplied by the NASA Ames GCM, would capture the tide as it entered and departed the domain. The GCM has trouble capturing the observed pressure cycle amplitude but does have tidal signatures. Therefore, it is unrealistic to expect MRAMS to reproduce the higher observed amplitude given the initial and boundary conditions. Supplying GCM-derived boundary conditions more frequently than every six hours may help simulate the tide.

Two-dimensional simulations of flow over a simple mountain barrier, and three-dimensional simulations over a crater similar to Big Crater, at the Mars Pathfinder landing site reveal that the atmospheric flow is significantly perturbed by topography. Effects include acceleration of the background wind in excess of three times the mean value, flow reversals, vertically propagating gravity waves, highly turbulent wake flows, and enhanced regions of atmosphere–surface interactions. In particular, the results demonstrate that modest topographic barriers are sufficient to generate surface winds capable of removing and transporting dust. The numerical results are in agreement with theory.

A large eddy simulation provided a look at the structure and behavior of the convective layer. Prior to and shortly after sun-

rise, the boundary layer is dominated by mechanical mixing, where weak shear parallel circulations dominate. As the nocturnal inversion erodes and the atmosphere becomes unstable, there is a rapid transition from mechanical to buoyancy-driven mixing. Narrow plumes surrounded by broad subsidence ascend to approximately 4 km. Turbulent statistics indicate that the turbulence is much more intense than that typically found on Earth, but that the fluxes are roughly an order of magnitude smaller due to the lower density of Mars' atmosphere. Vertical flux of horizontal momentum is intriguing as it did not have a consistent or coherent pattern, and it indicated periods of counter-gradient momentum transport. The mechanism for this has not yet been identified.

Emerging from the large eddy simulation were dust-devil-like circulations. The scale of the modeled phenomena seem to be slightly larger than observed, but this may be partially due to the inability of fully determine the size of a dust devil circulation based solely on the visual dust boundaries. The modeled circulation was roughly a few hundred meters wide and extended approximately 1.5 km vertically. Based on the population and frequency of the modeled circulations, it was estimated that at any particular time during the afternoon, there were roughly 0.03 to 0.1 per km^2. The modeled wind speed and pressure perturbations agree very well with the observations. Future studies will focus on the lifecycle and dynamics of the circulations.

APPENDIX: MATHEMATICAL NOTATION

Symbol	Meaning
u	East-west wind component
v	North-south wind component
w	Vertical velocity
$\pi = \frac{C_p T}{\theta}$	Exner function
f	Coriolis parameter
θ	Potential temperature
T	Temperature
$C_p = 860$ J Kg^{-1} K^{-1} (atmosphere)	Heat capacity at constant pressure for atmosphere or soil (variable value)
r	Tracer species
$\mathbf{K}_h, \mathbf{K}_m$	Vector momentum and thermal mixing coefficients
K_m, K_h	Momentum and thermal mixing coefficients (may be different in different directions as determined by $\mathbf{K}_h, \mathbf{K}_m$)
K_e	Mixing coefficient for turbulent kinetic energy
$R = 192$ J Kg^{-1} K^{-1}	Dry gas constant
$C_v = C_p - R$	Heat capacity at constant volume
C_x, C_z	Turbulence constants for horizontal and vertical diffusion, respectively. Values are set by user. Typical values: 0.2
$\alpha = \frac{K_h}{K_m}$	Ratio of mixing coefficients. Value is set by user. Typical value: 3.0
F_H	Binary parameter to invoke stability enhancement in vertical diffusion. $F_H = 1$ indicates scheme is active.
R_i	Richardson number

$N^2 = g\frac{d\ln\theta}{dz}$	Brünt–Väisälä frequency
$g = 3.72 \text{ m s}^{-2}$	Gravitational acceleration
K^*	Minimum horizontal momentum mixing coefficient
K_A	User-specified constant used in computing K^*. Typical values: 0.1–2.0
S_3	Magnitude of the rate-of-strain tensor
S_H	Magnitude of the rate-of-strain tensor taking into account only horizontal contributions
e	Turbulent kinetic energy (TKE)
l, l_∞	Mixing length scales
a_ε	Dissipation constant for TKE
k	Von Karman constant or soil thermal conductivity
z_o	Roughness length
S_m, S_h	Nondimensionalized expressions involving gradients of u, v, and θ. Used in the closure of the TKE equation.
u_*	Friction velocity
F_h, F_m	Atmospheric structure functions used in computing surface layer stresses
ε	Soil emissivity (user-specified)
σ	Steffan–Boltzman constant or Sigma–height coordinate
F	Energy flux
$SW\downarrow, LW\downarrow$	Downward short- and long-wave radiation at the surface
T_s	Soil temperature
$Z_T, topo_R$	Topography height in MRAMS
H	Model top or height above MRAMS topography at which MRAMS and GCM atmospheric structure are assumed identical
c	Speed of sound
Δ_{topo}	Difference in topography between MRAMS and GCM
Z	Height above the reference geoid
ρ	Density

ACKNOWLEDGMENTS

REFERENCES

Andre, J. C., G. De Moor, P. Lacarrere, and R. Du Vachat 1978. Modeling the 24 hour evolution of the mean and turbulent structures of the planetary boundary layer. *J. Atmos. Sci.* **35**, 1861–1883.

Barnes, J. R., J. B. Pollack, R. M. Haberle, C. B. Leovy, R. W. Zurek, H. Lee, and J. Schaeffer 1993. Mars atmospheric dynamics as simulated by the NASA Ames general circulation model, Part II: Transient baroclinic eddies. *J. Geophys. Res.* **98**, 3125–3148.

Blumsack, S. L., P. J. Gierasch, and W. R. Wessel 1973. An analytical and numerical study of the martian planetary boundary layer over slopes. *J. Atmos. Sci.* **30**, 66–82.

Bridger, A. F. C., and J. R. Murphy 1998. Mars' surface pressure tides and their behavior during global dust storms. *J. Geophys. Res.* **103**, 8587–8601.

Bridges, N., R. Greeley, A. F. C. Halderman, K. E. Herkenoff, M. Kraft, T. J. Parker, and A. W. Ward 1999. Ventifacts at the Pathfinder landing site. *J. Geophys. Res.* **104**, 8595–8615.

Bussinger, J. A., J. C. Wyngaard, Y. Izumi, and E. F. Bradley 1971. Flux–profile relationships in the atmospheric surface layer. *J. Atmos. Sci.* **28**, 191–189.

Christiansen, P. R., and H. J. Moore 1992. The martian surface layer. In *Mars* (H. Kieffer, B. M. Jakosky, C. W. Snyder, and M. S. Matthews, Eds.), pp. 686–727. Univ. of Arizona Press, Tucson.

Clark, T. L., and R. D. Farley 1984. Severe downslope windstorm calculations in two and three spatial dimensions using anelastic interactive grid nesting: A possible mechanism for gustiness. *J. Atmos. Sci.* **41**, 329–350.

Collins, M., and I. N. James 1995. Regular baroclinic transient waves in a simplified global circulation model of the martian atmosphere. *J. Geophys. Res.* **100**, 14,421–14,432.

Collins, M., S. R. Lewis, P. L. Read, and F. Hourdin 1996. Baroclinic wave transitions in the martian atmosphere. *Icarus* **120**, 344–357.

Davies, H. C. 1983. Limitations of some common lateral boundary schemes used in regional NWP models. *Mon. Wea. Rev.* **111**, 1002–1012.

Deardorff, J. W. 1972. Numerical investigation of neutral and unstable planetary boundary layers. *J. Atmos. Sci.* **29**, 91–115.

Durran, D. R. 1986. Mountain waves. In *Mesoscale Meteorology and Forecasting* (P. S. Ray, Ed.), pp. 472–492. Am. Meteorol. Soc.

Forget, F., F. Hourin, R. Fournier, C. Hourin, O. Talagrand, M. Collins, S. R. Lewis, P. L. Read, and J. P. Hout 1999. Improved general circulation models of the martian atmosphere from the surface to above 80 km. *J. Geophys Res.* **104**, 24,155–24,175.

Gierasch, P. J., and R. M. Goody 1968. A study of the thermal and dynamical structure of the lower martian atmosphere. *Planet. Space Sci.* **16**, 615–646.

Greeley, R. N., J. D. Iversen, J. B. Pollack, N. Udovich, and B. White 1974. Wind tunnel simulations of light and dark streaks on Mars. *Science* **183**, 847–849.

Greeley, R. N., R. Leach, B. White, J. Iverson, and J. Pollack 1980. Threshold windspeeds for sand on Mars: Wind tunnel simulations. *Geophys. Res. Lett.* **7**, 121–124.

Greeley, R. N., M. Kraft, R. Sullivan, G. Wilson, N. Bridges, K. Herkenhoff, R. O. Kuzmin, M. Malin, and W. Ward 1999. Aeolian features and processes at the Mars Pathfinder landing site. *J. Geophys. Res.* **104**, 8573–8584.

Haberle, R. M., C. B. Leovy, and J. B. Pollack 1982. Some effects of global dust storms on the atmospheric circulation of Mars. *Icarus* **50**, 322–367.

Haberle, R. M., H. C. Houben, R. Hertenstein, and R. Herdtle 1993a. A boundary-layer model for Mars: Comparison with Viking Lander entry data. *J. Atmos. Sci.* **50**, 1545–1559.

Haberle, R. M., J. B. Pollack, J. R. Barnes, R. W. Zurek, C. B. Leovy, J. R. Murphy, H. Lee, and J. Schaeffer 1993b. Mars atmospheric dynamics as simulated by the NASA-Ames general circulation model I. The zonal mean circulation. *J. Geophys. Res.* **98**, 3093–3123.

Haberle, R. M., M. M. Joshi, J. R. Murphy, J. R. Barnes, J. T. Schofield, G. W. Wilson, M. Lopez-Valverde, J. L. Hollingsworth, A. F. C. Bridger, and J. Schaeffer 1999. General circulation model simulations of the Mars Pathfinder atmospheric structure investigation/meteorology data. *J. Geophy. Res.* **104**, 8957–8974.

Hadfield, M. G., W. R. Cotton, and R. A. Pielke 1991. Large-eddy simulations of thermally forced circulations in the convective boundary layer. Part I: A small-scale circulation with zero wind. *Bound.-Layer Meteorol.* **57**, 79–114.

Klemp, J. B., and R. B. Wilhelmson 1978. The simulation of three-dimensional convective storm dynamics. *J. Atmos. Sci.* **35**, 1070–1096.

Leovy, C. B., and Y. Mintz 1969. Numerical simulation of the atmospheric circulation and climate of Mars. *J. Geophys. Res.* **26**, 1167–1190.

Lewellen, W. S., and M. Teske 1973. Prediction of the Monin–Obukhov similarity functions from an invariant model of turbulence. *J. Atmos. Sci.* **30**, 1340–1345.

Lewis, S. R., M. Collins, P. L. Read, F. Forget, F. Hourin, R. Fournier, C. Hourin, O. Talagrand, and J.-P. Huot 1999. A climate database for Mars. *J. Geophys. Res.* **104**, 24,177–24,194.

Louis, J. F. 1979. A parametric model of vertical eddy fluxes in the atmosphere. *Bound.-Layer Meteorol.* **17**, 187–202.

Magalhães, J. A., and P. Gierasch, 1982. A model of martian slope winds: Implications for Aeolian transport. *J. Geophys. Res.* **87**, 9975–9984.

Magalhães, J. A., and R. E. Young 1995. Downslope windstorms in the lee of ridges on Mars. *Icarus* **113**, 277–294.

Manton, M. J., and W. R. Cotton 1977. Parameterization of the atmospheric surface layer. *J. Atmos. Sci.* **34**, 331–334.

Mason, P. J. 1989. Large-eddy simulation of the convective atmospheric boundary layer. *J. Atmos. Sci.* **46**, 1492–1516.

Mellor, G. L., and T. Yamada 1982. Development of a turbulence closure model for geophysical fluid problems. *Rev. Geophys. Space Phys.* **20**, 851–875.

Metzger, S. M., J. R. Carr, J. R. Johnson, T. J. Parker, and M. T. Lemmon 1999. Dust devil vortices seen by the Mars Pathfinder camera. *J. Geophys. Res. Lett.* **26**, 2781–2784.

Mintz, Y. 1961. The general circulation of planetary atmospheres. In *The Atmospheres of Mars and Venus* (W. W. Kellog and C. Sagan, Eds.), NAS–NRC 944, 107–146.

Orlanski, I. 1976. A simple boundary condition for unbounded hyperbolic flows. *J. Comput. Phys.* **21**, 251–269.

Pielke, R. A. 1984. *Mesoscale Meteorological Modeling*, p. 323. Academic Press, San Diego.

Pielke, R. A., W. R. Cotton, R. L. Walko, C. J. Tremback, W. A. Lyons, L. D. Grasso, M. E. Nicholls, M. D. Moran, D. A. Wesley, T. J. Lee, and J. H. Copeland 1992. A comprehensive meteorological modeling system—RAMS. *Meteorol. Atmos. Phys.* **49**, 69–91.

Pollack, J. B. D., R. M. Haberle, J. Schaeffer, and H. Lee 1990. Simulations of the general circulation of the martian atmosphere I: Polar processes. *J. Geophys. Res.* **95**, 1447–1474.

Ryan, J. A., and R. D. Lucich 1983. Possible Dust devils, vortices on Mars. *J. Geophys. Res.* **88**, 11,005–11,011.

Savijärvi, H., and T. Siili 1993. The Martian slope winds and the nocturnal PBL jet. *J. Atmos. Sci.* **50**, 77–88.

Schmidt, H., and U. Schumann 1989. Coherent structure of the convective boundary layer derived from large-eddy simulations. *J. Fluid Mech.* **200**, 511–562.

Schneider, J. M. 1991. *Dual Doppler Measurement of a Sheared Convective Boundary Layer*. Ph.D. thesis, The University of Oklahoma, Norman, OK.

Schofield, J. T., J. R. Barnes, D. Crisp, R. M. Haberle, S. Larsen, J. A. Magalhães, J. R. Murphy, A. Seif, and G. Wilson 1997. The Mars Pathfinder atmospheric structure investigation/meteorology (ASI/MET) experiment. *Science* **278**, 1752–1758.

Seiff, A., and D. B. Kirk 1977. Structure of the atmosphere of Mars in summer at mid-latitudes. *J. Geophys. Res.* **82**, 4364–4378.

Seiff, A. 1993. Mars atmospheric winds indicated by motion of the Viking landers during parachute descent. *J. Geophys. Res.* **98**, 7461.

Siili, T., R. M. Haberle, and J. R. Murphy 1997. Sensitivity of martian southern polar cap edge winds and surface stresses to dust optical thickness and to the large-scale sublimation flow. *Adv. Space. Res.* **19**, 1241–1244.

Sinclair, P. C. 1966. *A Quantitative Analysis of the Dust Devil*. Ph.D. thesis, University of Arizona, Tucson.

Smagorinsky, J. 1963. General circulation experiments with the primitive equations. Part I: The basic experiment. *Mon. Wea. Rev.* **91**, 99–164.

Thomas, P. 1984. Martian intracrater splotches: Occurrence, morphology, and colors. *Icarus* **57**, 205–227.

Thomas, P., J. Veverka, D. Gineris, and L. Wong 1984. "Dust" streaks on Mars. *Icarus* **60**, 161–179.

Thomas, P., and P. J. Gierasch 1985. Dust devils on Mars. *Science* **230**, 175–177.

Tremback, C. J., J. Powell, W. R. Cotton, and R. A. Pielke 1987. The forward-in-time upstream advection scheme: Extension to higher orders. *Mon. Wea. Rev.* **115**, 540–555.

Tripoli, G. J., and W. R. Cotton 1982. The Colorado State University three-dimensional cloud/mesoscale model. Part I: General theoretical framework and sensitivity experiments. *J. Res. Atmos.* **16**, 185–220.

Veverka, J. 1975. Variable features on Mars V: Evidence for crater streaks produced by wind erosion. *Icarus* **25**, 595–601.

Veverka, J., P. J. Gierasch, and P. Thomas 1981. Wind streaks on mars: Meteorological control of occurrence and mode of formation. *Icarus* **45**, 154–166.

Wilson, R. J., and K. Hamilton 1996. Comprehensive model simulation of the thermal tides in the martian atmosphere. *J. Atmos. Sci.* **53**, 1290–1326.

Wilson, R. J. 1997. A general circulation model simulation of the martian polar warming. *Geophys. Res. Lett.* **24**, 123–126.

Ye, Z. J., M. Segal, and R. A. Pielke 1990. A comparative study of daytime thermally induced upslope flow on Mars and Earth. *J. Atmos. Sci.* **47**, 612–648.